Electrochimica Acta 566 (2026) 148794

Contents lists available at ScienceDirect

Electrochimica Acta

journal homepage: www.journals.elsevier.com/electrochimica-acta

Development of partially hydrophobic surfaces to enhance the efficiency and durability of electrodes for alkaline water electrolysis

Juan D. Arias, Santiago Cartagena, Simón Quiroz, Jorge A. Calderón *

Centro de Investigación, Innovación y Desarrollo de Materiales – CIDEMAT, Universidad de Antioquia, Cr. 53 No 61 – 30, Torre 2, Lab. 330, Medellín, Colombia

ARTICLE INFO

Keywords:
Hydrogen evolution
Oxygen evolution
Water splitting
Overpotential
Hydrophobic electrode
Catalytic coating

ABSTRACT

Hydrogen gas is a fuel with a reduced environmental impact, and its production is currently promoted by water electrolysis. However, the growth and release of bubbles on the surface of electrodes involved in hydrogen and oxygen evolution reactions (HER and OER) affect the overpotential of the electrolysis process. Therefore, the study of gas bubble behavior and management has become a crucial aspect to consider when seeking to improve energy efficiency in the water-splitting process. This work shows that integrating porous electrodes partially coated with hydrophobic material (PTFE) reduces overpotentials for both HER and OER, showing excellent catalytic activities in stationary tests. Physical characterization of electrodes indicates that the PTFE particles are distributed as nodules, providing a larger electrochemical surface area with low surface free energy. At a current density of 400 mA cm^{-2}, the PTFE-modified electrodes exhibit overpotentials of 193 mV for HER and 230 mV for OER, compared to 230 mV and 278 mV, respectively, for the electrodes without PTFE. Furthermore, the full cell assembled with PTFE-modified electrodes achieves a low operating voltage of 1.70 V at 400 mA cm^{-2}

1. Introduction

Climate change, the depletion of fossil fuels, and the growth in demand for energy, coupled with greenhouse gas emissions, have opened possibilities to implement emerging energy systems. However, the energy of these systems can often not be generated continuously, so a method of energy storage is necessary. Likewise, many industrial processes use fossil fuels, which can be difficult to electrify. Green hydrogen has stood out as a promising option in the transition to renewable energy storage and the decarbonization of many industries. Unlike conventional hydrogen, which is often produced from natural gas and emits carbon dioxide, green hydrogen is produced using electrolysis methods powered by renewable energy [1]. The electrolysis process involves splitting water into two components (hydrogen and oxygen) using renewable energy sources such as wind, solar, and others [2,3]. For this reason, it is essential to make the process more efficient and economical [4,5].

Considering the above scenario, the reactions involved in water splitting, namely the hydrogen evolution reaction (HER) and the oxygen evolution reaction (OER, exhibit low efficiency, especially at high current densities. In practical alkaline electrolysis, the OER is widely recognized as the main kinetic bottleneck because it involves sluggish multi-electron transfer steps and therefore requires a larger overpotential, whereas the HER is generally faster [6]. Nevertheless, significant improvement of the HER is still required, particularly through the development of alternative catalysts to replace Pt. This need arises from the intrinsic activation energy barrier, gas bubble formation, and the gradual reduction in reaction rate over time, which together remain major challenges in water electrolysis [1,7]. To improve this low efficiency, the electrodes are coated with catalytic materials, seeking to improve the catalytic activity and increase the electrochemical surface area (ECSA) [8–10]. However, the surface area can be blocked if the gas bubbles produced during the reactions do not detach easily or quickly enough from the electrode surface, accumulating and merging [11]. When there is a high coverage of bubbles, the necessary interaction between the electrolyte and the electrode becomes difficult, resulting in a decrease in the surface area available. In addition, the ionic diffusion resistance increases, which negatively affects the performance of the electrode. Following the above, the bubble formation process can be described as a cycle of four stages: bubble nucleation, growth, subsequent detachment from the electrode surface, and finally, transport of the bubbles away from the space between the electrodes [11–13]. Increasing attention has been paid to the difficulties associated with bubble formation in the water electrolysis process. Reducing the size of

* Corresponding author.
E-mail address: andres.calderon@udea.edu.co (J.A. Calderón).

https://doi.org/10.1016/j.electacta.2026.148794
Received 5 February 2026; Received in revised form 27 March 2026; Accepted 30 March 2026
Available online 2 April 2026
0013-4686/© 2026 The Authors. Published by Elsevier Ltd. This is an open access article under the CC BY-NC-ND license (http://creativecommons.org/licenses/by-nc-nd/4.0/).

gas bubbles during detachment would prevent the previously mentioned drawbacks. In addition, different alternative catalytic coatings have been developed to reduce the HER and OER overpotentials for fresh and seawater electrolysis. Ren et al. [14] developed Ag-NiCrLDH-0.3 catalyst which displayed overpotentials at 10 mA cm^{-2} of 275.5 mV and 116.5 mV for OER and HER, respectively. Zhang et al. [15] proposed a Co0.5Ni0.5Se2@NiFe-LDH heterostructured catalyst exhibiting HER and OER overpotentials at 50 mA cm^{-2} of 219 mV and 247 mV, respectively. Zhang et al. [16] commented that the FeSe/NiP-600 catalyst exhibits HER and OER overpotentials of 122.7 mV at −10 mA cm^{-2} and 208 mV at 50 mA cm^{-2}. Zhou et al. [17] synthesized CoSe/$NiSe_2^{-3}$ nanosheets which exhibited OER overpotentials at 10 mA cm^{-2} for fresh water and seawater of 215.3 mV and 250.5 mV, respectively. However, those results are not sufficient for real electrolyzer applications because higher current densities, equal or larger than 400 mA cm^{-2} and longer electrolysis tests are required.

Various strategies and design efficiency innovations to minimize direct losses in the water electrolysis process within an electrolyzer have been described. These strategies include creating hydrophobic sites on electrode surfaces to control the formation and release of bubbles [18] and the development of superhydrophilic surfaces that are highly attractive to water. The bubble–surface interaction strongly depends on wettability. On hydrophobic sites, gas nuclei are energetically favored, and bubbles tend to spread and coalesce, which can promote bubble growth and facilitate removal by buoyancy-driven departure, but may also increase bubble coverage if detachment is delayed. In contrast, hydrophilic and especially superhydrophilic surfaces retain a stable hydration layer that minimizes direct gas–solid contact, leading to a large underwater bubble contact angle and a much lower adhesion force, so bubbles detach rapidly at smaller sizes [19,20]. This superhydrophilicity enhances the dispersion and release of bubbles, enabling them to separate quickly with a small size after formation, and the electrodes can be fabricated using various materials and techniques [19]. In addition, efforts are being made to configure and modify a wetting surface morphology on electrodes to accelerate and control bubble dynamics and nucleation [21]. Implementing the capillary feed improves the energy efficiency of the water electrolysis cell [22]. Other approaches involve applying ultrasound to the electrolyte to facilitate bubble detachment and mass transport [23]. The use of magnetic fields and supergravity within the electrolyzer to keep the catalytic space of the electrodes free of bubbles is being explored. This involves assisting neighboring bubbles in detaching from hydrophobic sites, although the effect on isolated bubbles is insignificant [24–26].In addition, rapid pumping at the electrode surfaces separates bubbles as they form. Introducing a flow field helps accelerate bubble detachment by improving contact between the catalysts and the electrolyte, allowing the electrolyte to flow through the electrode pores [27]. Modifications to the liquid electrolyte and its interface with the electrode surface are aimed at facilitating bubble nucleation and detachment. Finally, applying continuous modify changes dynamically modifies bubble buoyancy [7,11–13,28].

However, many methods require external equipment that can increase the cost of the process. Also, the use of new deposition methods depends on the implementation of changes in the synthesis of the material, creating additional development costs. The use of hydrophobic particles would appear to be a low-cost and straightforward process; a few works by different authors have demonstrated that hydrophobic surfaces, particularly those formed by polytetrafluoroethylene (PTFE) particles, can induce coalescence and assist in transporting newly formed gas bubbles in both the oxygen evolution reaction (OER) [28,29] and hydrogen evolution reaction (HER) [30] in water splitting processes. Due to the high electronegativity, low polarizability, low surface energy, and small van der Waals radius of the fluorine atom, fluorinated polymers exhibit outstanding properties for various applications. PTFE particles are highly hydrophobic, allowing the surface to repel water and imparting various properties that enable diverse applications such as self-cleaning and anti-fouling surfaces [31]. Similarly, due to their wide availability, variety, and low cost, PTFE particles are quickly stabilized using surfactants [32] and can be easily used to create hydrophobic areas. For this reason, we modified two synthesis routes previously developed in-house to integrate particles of PTFE in the electrodeposition of cheap and abundant catalytic metals.

This work presents an innovative approach to the design of electrodes for water electrolysis by incorporating hydrophobic PTFE particles into nickel-iron layered double hydroxide (NiFeLDH) and nickel phosphide (NiP) coatings. The partial surface modification combines hydrophilic and hydrophobic regions, resulting in a significant improvement in the efficiency of the OER and HER. The incorporation of PTFE particles into the metallic coatings was achieved through optimized electrodeposition processes using controlled stirring rates that promote homogeneous co-deposition of the hydrophobic material. Unlike other techniques that require complex treatments or the use of expensive materials to achieve hydrophobic coatings, the electrodeposition method uses accessible inputs and simple procedures, enabling low-cost industrial scalability. In addition, two simple electrolytic baths were used to obtain NiP-PTFE and NiFeLDH-PTFE coatings on nickel foams. This procedure made it possible to evaluate the influence of the PTFE content on the adhesion, stability, and catalytic behavior of the coatings for general water splitting, which was judged based on the performance obtained in the electrochemical curves and visually based on the detachment of particles at the bottom of the electrolyte during the respective evaluations. The results of the coated electrodes were also compared with the performance of the nickel foam without PTFE, thus demonstrating the advantages of using PTFE particles in the coatings. This type of dispersed phase coating is not a widely used strategy when performing HER and OER reactions. Moreover, it is novel in that the versatility of PTFE allows it to be used on a wide variety of catalysts already developed, and it does not involve high additional costs.

2. Experimental

2.1. Materials and reagents

2.1.1. Electrodeposition of Ni and Ni-PTFE compounds

Electrodeposition of Ni with PTFE compounds was carried out to observe the effect of PTFE particles in combination with conductive materials and thus determine the optimal PTFE particle concentration in electrochemical baths. A Watts bath was used, containing 240 g/L of $NiSO_4 \cdot 6H_2O$ (EMSURE® MERCK, ≥99.0 %), 30 g/L of $NiCl_2 \cdot 6H_2O$ (EMSURE® MERCK, ≥98.0 %), and 30 g/L of H_3BO_3 (ALDRICH, ≥99.5 %). All reagents were of analytical grade. Nickel sheets (3 cm × 1 cm) were used as the cathode material. Commercial PTFE particles ($(C_2F_4)_n$) with diameters of 10 and 20 um were used, and hexadecyltrimethylammonium bromide $C_{19}H_{42}BrN$ (ALDRICH, ≥98 %) was used as surfactant. The nickel sheets were polished with 1000-grit silicon carbide sandpaper and subsequently cleaned in ethanol for 5 min using ultrasonic agitation. Nickel sheets were also employed as the anode material.

During the electrodeposition process, the anode and cathode were positioned vertically and in parallel, maintaining a separation of 2–3 cm. To ensure proper bath agitation and adequate dispersion of the particles, a magnetic stirrer was used. The amount of PTFE in the electrolytic bath was varied to obtain coatings with different wettability characteristics. The PTFE particle concentration range was set between 5 and 40 g/L. The polymeric particles were dispersed in an aqueous medium using a surfactant (see Section 2.2). Once complete dispersion was achieved, the electrochemical bath components were added to the PTFE dispersion. Ni-PTFE coatings were electrodeposited by applying a current density of −40 mA·cm^{-2} to the working electrode for 2400 s. The bath pH was adjusted to 4.5 with sulfuric acid to enhance stability. Bath agitation was maintained between 400 and 600 RPM. After deposition, the samples with varying PTFE concentrations were ultrasonically cleaned in ethanol

for 5 min at room temperature. Finally, the electrodes were rinsed with distilled water.

2.1.2. Electrodeposition of NiFeLDH and NiP with and without PTFE

The following is a list of the reagents used in the experiments, all of which were analytical grade: $NiNO_3 \bullet 6H_2O$ (Thermo scientific ≥98 %), NaCl (Sanal®P ≥ 99.7 %), $NaH_2PO_2.\bullet H_2O$ (ALDRICH, ≥99 %), $NiSO_4 \bullet 6H_2O$ (≥ 99.0 %), $Na_3C_6H_5O_7$ (≥ 99.0 %), and $FeNO_3 \bullet 9H_2O$ (≥ 99.0 %). The last two of these were purchased from EMSURE® MERCK and used for the electrochemical baths of the NiP and NiFeLDH coatings respectively. Commercial nickel foams with dimensions of approximately 1 cm x 3 cm x 0.16 cm from Xiamen Tmax Battery Equipments Limited were used as working substrate.

2.2. PTFE dispersion

PTFE particles were added to the electrochemical bath at concentrations ranging from 5 to 40 g L^{-1}. These particles were dispersed in deionized water using a cationic surfactant, cetyltrimethylammonium bromide (CTAB), at a concentration of 0.033 g/g PTFE. It has been shown that this type of cationic surfactant can adsorb onto the particles and provide a positive charge on their surface. This increases the electrostatic repulsion between the particles, preventing their aggregation and improving the dispersion of the particles in the solution. In this way, a more homogeneous distribution of the particles on the electrode surface is achieved [31]. The PTFE particles were first dispersed in deionized water for 15 min using a magnetic stirrer to agitate the bath and maintain particle dispersion. The dispersion was then subjected to ultrasonic agitation for 45 min to break up larger agglomerates in the PTFE powder. Once the particles were fully dispersed, the electrochemical bath components were added to the PTFE dispersion.

2.3. NiP-PTFE and NiFeLDH-PTFE coating preparation

The electrodeposition of the coatings was carried out under the following conditions and using the specified reagents. Nickel foam substrates were cleaned with distilled water, followed by immersion in 3 M HCl in an ultrasonic bath, and then rinsed with distilled water.

2.3.1. NiP-PTFE cathodic coating

The electrodeposition of the NiP-PTFE catalyst was performed using a graphite electrode as the counter electrode, applying a current density of −30 mA cm^{-2} to the working electrode for 40 min. The electrolytic bath consisted of 0.15 M $NiSO_4 \cdot 6H_2O$, 0.15 M $NaH_2PO_4 \cdot H_2O$, 0.19 M $Na_3C_6H_5O_7 \cdot 2H_2O$, and 0.28 M NaCl, with distilled water as the solvent. The bath pH was adjusted to 7.5 using a 25 % ammonia solution. The temperature was maintained between 25 and 30 °C.

2.3.2. NiFeLDH-PTFE anodic coating

The electrodeposition of NiFeLDH-PTFE was carried out using $Ni(NO_3)_2 \cdot 6H_2O$ and $Fe(NO_3)_3 \cdot 9H_2O$ salts in a 15:1 molar ratio, with concentrations of 14.0625 mmol and 0.9375 mmol, respectively. A three-electrode cell was employed, consisting of an Ag/AgCl reference electrode, a platinum mesh counter electrode, and nickel foam with the respective coating as the working electrode. The deposition potential was set at −1.014 V vs. Ag/AgCl. The deposition was conducted at room temperature for 40 min under continuous agitation to control hydrodynamic mass transport and to keep PTFE particles suspended, while maintaining the bath pH at 2.0.

2.3.3. PTFE codeposition and hydrodynamic control (applies to both anode and cathode coatings)

To systematically evaluate the effect of agitation on PTFE stability and incorporation during composite codeposition, both the NiFeLDH-PTFE anodic coating and the NiP-PTFE cathodic coating were prepared under magnetic stirring at 200, 300, 450, 600, 900, and 1200 rpm, and these conditions were also selected to promote good coating adhesion. The PTFE concentration used for the codeposition of polymeric particles in the catalytic layers was fixed at 30 g L^{-1}, as determined from the wettability response of Ni–PTFE coatings. In addition, stirring enhanced bath homogenization, improved particle transport toward the cathode surface, and increased the deposition rate [33]. To ensure comparable hydrodynamic conditions across experiments, the working electrode was positioned at a fixed distance from the stir bar, and both the electrolyte volume and stir-bar dimensions were kept constant. These parameters are known to affect local flow fields and particle entrapment during composite codeposition, thereby influencing PTFE loading and coating morphology [34]. After electrodeposition, the coated samples were ultrasonically washed in ethanol for 5 min to remove residual surfactant that could interfere with electrochemical evaluation. Finally, the electrodes were thoroughly rinsed with distilled water.

2.4. Characterization

The surface morphology and distribution of PTFE particles in all composite coatings were examined by scanning electron microscopy (SEM) using a JEOL-JSM 6490LV instrument with an acceleration voltage of 20 kV. Elemental composition analysis was performed by energy-dispersive X-ray spectroscopy (EDS). Raman spectra of the surfaces were obtained with a microscope in the scanning range from 100 to 3000 cm^{-1}, using a HORIBA JOBIN YVON LabRAM HR confocal micro-Raman spectroscope integrated with a 633 nm helium-neon laser with a power of 17 mW. Attenuated total reflectance analysis by Fourier transform infrared spectroscopy (FTIR-ATR) was performed using a PerkinElmer spectrum of two infrared spectrophotometers with a resolution of 8 cm^{-1} over 400 to 4000 cm^{-1}. The wettability properties of the initial samples on nickel sheets were determined by measuring the contact angle with deionized water droplets resting on the surface. A Ramé-Hart model 250 goniometer/tensiometer was used for this purpose. To study the evolution and composition of PTFE in the NiP and NiFeLDH catalytic coatings, thermogravimetric analyses (TGA) were performed using a Q500 device from TA Instruments. The samples were placed in a nitrogen atmosphere and heated from room temperature to 850 °C at a heating rate of 10 °C min^{-1}.

2.5. Electrochemical test

Electrochemical experiments for the (HER) and (OER) reactions were carried out using a 1 M NaOH solution and an AUTOLAB PGSTAT302F potentiostat-galvanostat. A three-electrode cell configuration was used, consisting of a working electrode, which was foam coated with the catalytic material, an Hg/HgO electrode (made in-house) as reference electrode, and finally, a graphite rod as counter electrode. The electrolyte was replaced with a fresh solution for each electrochemical experiment. The electrochemical evaluation of the coatings consisted of determining their capacitance, catalytic power, and the kinetics of the reactions involved in the process (HER and OER). Cyclic voltammetry (CV) was performed for all coatings to obtain the electrochemical double layer capacitances (Cdll) in a non-faradic region at different sweep rates of 10, 20, 40, 60, 80, 100, 120 mVs^{-1} in 5 cycles per rate to obtain constant values, in a window around the open circuit potential (OCP). Linear sweep voltammetry (LSV) for HER and OER were evaluated with a linear sweep from 0.3 V to 1.1 V vs. Hg/HgO for OER and from −0.7 V to −1.9 V vs. Hg/HgO for HER at a scan rate of 5 mV s^{-1}. Tafel plots were constructed from potentiodynamic polarization measurement performed at a scan rate of 80 μV s^{-1}. Overpotentials were calculated according to literature reports [35,36], Eq. (1):

$$\eta = \varepsilon_m + \varepsilon_{ref}/H_2 + 0.059V \times \mathrm{pH} - R_{sln} \times I- \quad (1)$$

Where ε_m is the potential difference between the evaluated electrode

and the reference electrode, ε_{ref} is the potential difference between the reference electrode and the standard hydrogen electrode, R_{sln} is the solution resistance with regard to the electron flow during the test, I is the current response generated in the system, and finally, ε_{eq} is the equilibrium potential of the reaction involved (1.23 V for OER and 0 V for HER) [36]. Coating detachment was also evaluated over extended periods for the best coatings to evaluate the adhesion and durability of the coating. This stability test consisted of the application of a high constant current density of ±400 mAcm^{-2} for 24 h. This was performed on the coating with PTFE and without PTFE to check for changes in the catalytic capacity of the electrodes. Electrochemical impedance spectroscopy (EIS) measurements were performed to understand the interactions that may occur between the electrode surface and the electrolyte. Measurements were performed over 100 kHz to 10 mHz frequency range using a Zhaner IM6 potentiostat, polarized at potentials of 0.564 and −1.130 V vs. Hg/HgO for the anodic and cathodic reactions, respectively. Catalysts and electrodes were prepared using the same methodology described above. The impedance spectrum was fitted to the equivalent circuit, and the equivalent capacitance values obtained from the EIS experiments were calculated using the Brug equation (Eq. (2)), which accounts for surface heterogeneities [37]. α and Q are the CPE parameters, R_e is the ohmic resistance, R_t is the charge transfer resistance, and C_{eff} is the effective capacitance.

$$Ceff = Q^{\frac{1}{\alpha}} \left(R_e^{-1} + R_t^{-1}\right)^{\frac{\alpha-1}{\alpha}} \quad (2)$$

The behavior and bubble size were studied in a three-electrode cell with 1 M NaOH solution at room temperature and a current density of ±50 mA/cm^2. Video images were recorded using a mobile device integrated with a 60x microscope.

3. Results and analysis

3.1. Contact angle and coating hydrophobicity evaluation

The dispersion of PTFE in the electrochemical bath significantly affects both the amount of co-deposited PTFE and the wettability properties of the coatings. Figure S1, in the supporting information, shows the contact angle values for coatings with different concentrations of PTFE in the electrolytic bath. It is observed that the hydrophobicity of the coating increases as the concentration of PTFE particles co-deposited increases. Table 1 shows the contact angle of coatings obtained by electrodeposition with different PTFE contents. Water contact angles vary with the amount of PTFE in the electrolytic bath, increasing with particle concentration up to a threshold value of 30 g L^{-1}, and reaching a value of to 148 ± 1.38°, see Table 1. This result indicates that the amount of co-deposited PTFE increases proportionally with the concentration in the bath, ranging from 5 g L^{-1} to a maximum of 40 g L^{-1}. These results demonstrate the potential for developing durable hydrophobic or superhydrophobic surfaces over time. Furthermore, the contact angles obtained in this study are comparable, and even higher than those obtained in other works reported in literature. For example, Lacovetta et al.[31]. reported a contact angle of about 152° with a superior PTFE content of 69 % by volume; Wang et al. [38] achieved values close to 155°; Isern et al.[39]. achieved angles of 114°, and Hui You et al. [34] reported a value of 121° However, Figure S1 shows a decrease in the contact angle when the PTFE concentration reaches 40 g L^{-1}, probably due to the formation of agglomerates caused by particle collisions at such high PTFE concentrations.

Table 1
Contact angle (θ), surface free energy of the coatings (γ_s) and the work of adhesion of solid-liquid interface (W_{sl}) values for coatings obtained with different PTFE concentrations.

Sample	PTFE Concentration (g L^{-1})	Contact Angle (°)	γ_s (mJ m^{-2})	W_{sl} (mJ m^{-2})
1	0	74 ± 3.14	39.2 ± 2.1	92.9 ± 2
2	10	91 ± 1.40	28.6 ± 0.8	71.5 ± 1.8
3	15	115 ± 2.28	14.3 ± 1.6	42.0 ± 1.4
4	20	125 ± 0.48	9.1 ± 0.4	31.0 ± 0.8
5	30	148 ± 1.38	1.5 ± 0.2	11.0 ± 0.6
6	40	138 ± 1.67	3.9 ± 0.4	18.7 ± 0.9

The surface free energy of the coatings (γ_s) can be calculated using the Neumann relationship, Eq. (3) [40]. The work of adhesion of the solid-liquid interface is calculated according to Eq. (4), which represents the work required to separate unit area of the solid-liquid interface. Those values are also presented in Table 1, for the coatings obtained at different PTFE content.

$$\cos\theta = 2\sqrt{\frac{\gamma_s}{\gamma_l}}\, e^{-\beta(\gamma_l-\gamma_s)^2} - 1 \quad (3)$$

$$W_{sl} = 2\sqrt{\gamma_l \gamma_s}\, e^{-\beta(\gamma_l-\gamma_s)^2} \quad (4)$$

Where, θ is the contact angle (°), γ_s is the surface free energy of the coating, γ_l is the surface tension of the water (72.8 mJ m^{-2}), W_{sl} is the work of adhesion of the solid-liquid interface, and β is an empirical constant equal to 0.0001247 (m^2 mJ^{-1})^2. As can be seen in Table 1, the surface free energy of the coating is reduced when PTFE particles are incorporated, reaching its lowest value of 1.5 ± 0.2 mJ m^{-2} at a PTFE concentration in the electrolytic bath of 30 g L^{-1}, which means that highest hydrophobicity is reached at that condition and water islands can be formed at the interface. Also, the work of adhesion of the solid-liquid interface is lowest in these conditions (11.0 ± 0.6 mJ m^{-2}), meaning that water islands can be easily moved by nascent gas bubbes, facilitating the nucleation and growth of bubbles at the interface when OER or HER occur.

Based on the results of the PTFE particle concentration and the corresponding contact angle, which measures the hydrophobicity of the Ni coatings, a concentration of 30 g L^{-1} was selected to obtain electrocatalytic composite coatings in further experiments, where NiP-PTFE and NiFeLDH-PTFE were tested for alkaline water splitting.

3.2. Chemical and structural characterization

The RAMAN analysis of the electrodeposited coated samples is

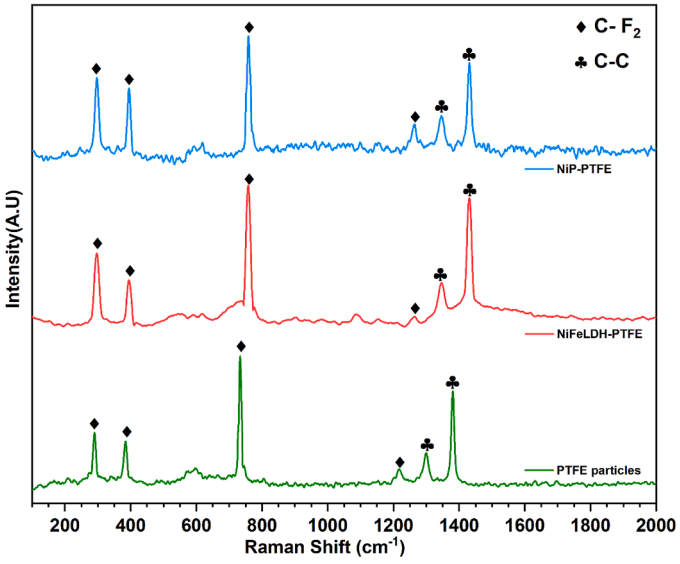

Fig. 1. Raman spectra obtained for the different NiP-PTFE and NiFeLDH-PTFE coatings.

shown in Fig. 1. PTFE exhibits several active modes in Raman, appearing at 290, 384, 733, 1217, 1300, and 1380 cm^{-1} [41,42]. The signals at 290 and 384 cm^{-1} are associated with CF_2 twisting and bending vibrations 734 cm^{-1} (symmetric stretching of CF_2), 1218 cm^{-1} (antisymmetric stretching of CF_2), 1302 cm^{-1}, and 1382 cm^{-1} (C—C stretching). These values agree with those reported in the literature [43,44]. In the spectra of PTFE, NiP-PTFE, and NiFeLDH-PTFE samples the observed peaks are in the ranges of active modes of PTFE. However, the Raman spectra of the catalytic material differ slightly from the spectrum of the pure PTFE because the composite materials exhibit broader bands, due to a possible increase in the visibility of the metal phases and a shift of the peaks towards higher wavenumbers due to changes in the vibrational modes caused by the interaction between the metals and PTFE. The Raman spectra confirm the presence of PTFE particles co-deposited with the coatings studied (Ni-P and NiFeLDH). It should be clarified that PTFE particles were co-deposited in the form of nodules and were not entirely dispersed with the NiFe or NiP in the coating matrix. Raman measurements were explicitly performed on the border between PTFE particles and the foam's pore, as will be shown later in the SEM images analysis.

Fig. S2 shows the Raman spectra obtained for the NiFe-LDH and NiP base coatings. For the NiFe-LDH (Fig. S2a) there is evidence of prominent bands between 214 cm^{-1} and 280 cm^{-1} associated with vibrations of Ni-Fe system [45]. There are also two representative bands of intense signal between 450 cm^{-1} and 700 cm^{-1}, in this case, attributed to vibrations of the disordered LDH structural network [45–47]. These vibrations correspond to Ni-Fe hydroxides and usually occur between metal and oxygen bonds [46]. The band's intensity indicates good particle deposition on the coating (NiFe-LDH), demonstrating that the catalyst underwent the appropriate chemical transformations to develop OER. Regarding the Raman spectrum of the NiP coating, no noticeable or significant bands are observed, indicating the metallic character of the developed coating. Regarding the Raman spectra performed, it should be clarified that different scans were performed on the evaluated coating systems for the same sample at various points of the surface to confirm the uniformity of the surface after the coating deposition process. Like the Raman analysis, the FTIR spectroscopy confirmed the presence of PTFE in the NiFeLDH-PTFE and NiP-PTFE composite coatings. Fig. 2 shows the characteristic bands of PTFE located at 540 −1213 cm^{-1} wavenumbers; those bands are also observed in the NiFeLDH-PTFE and NiP-PTFE composite coatings. Intense absorption bands are observed between 500 and 1200 cm^{-1}, where the strong signals at 1200 cm^{-1} and 1146 cm^{-1} are associated with stretching vibrations of the C-F bond, while the signal at 637 cm^{-1} is probably due to deformation vibrations of the C-F segment [48,49]. In NiFe-LDH coating the emerging absorption bands at about 3600–3200 cm^{-1} and 1636 cm^{-1} are related to the OH functional groups of LDH compound [50]. For NiP-PTFE coatings the FTIR spectrum showed only the characteristic bands corresponding to the C-F groups of the PTFE present in the sample, but with lower intensity. Raman and FTIR spectra show that PTFE particles are present and exposed in the superficial layer of the electrodeposited coatings.

SEM micrographs of the Ni-P and NiFe-LDH samples are shown in Fig. 3 and Fig. 4, respectively. A clear difference in coating growth and apparent mass loading is observed between both systems: the NiP deposit forms a relatively compact and conformal nodular layer on the Ni-foam ligaments, whereas the NiFe-LDH coating develops a much more voluminous, hierarchical platelet/nanosheet-like morphology that produces a thicker-looking deposit and a higher surface coverage, Additional SEM images provided in the Supplementary Information (Fig. S3) further highlight these differences with higher magnifications, where NiP (Fig. S3 a–b) exhibits a dense nodular structure decorated by flake-like structures, while NiFeLDH (Fig. S3 c–d) shows stacked plate-like domains and agglomerated nanosheets. Despite this more open and porous appearance, the layered structure of NiFeLDH may limit the electrochemical accessibility of the surface due to stacking and partial shielding of active sites. In contrast, the compact and nodular morphology of NiP provides a more uniformly accessible interface, with a high density of electrochemically connected sites that can be readily reached by the electrolyte as can be seen later with the calculation of the roughness factor (Rf). For clarity, the PTFE-rich domains are visible as micrometer-sized agglomerated nodules and are highlighted with red rectangles in Fig. 3(a–c) and Fig. 4(a–c). PTFE particles were dispersed in the form of nodules located on the outer edges of the pores of the nickel foam. PTFE particles are also present in the interior of the Ni foam, because of the periodic stirring performed during coating electrodeposition which pushed the PTFE particles near the foam into it. In turn, the surfactant stabilizes the PTFE in the suspension, helping the coating electrodeposition by increasing its net positive charge on the

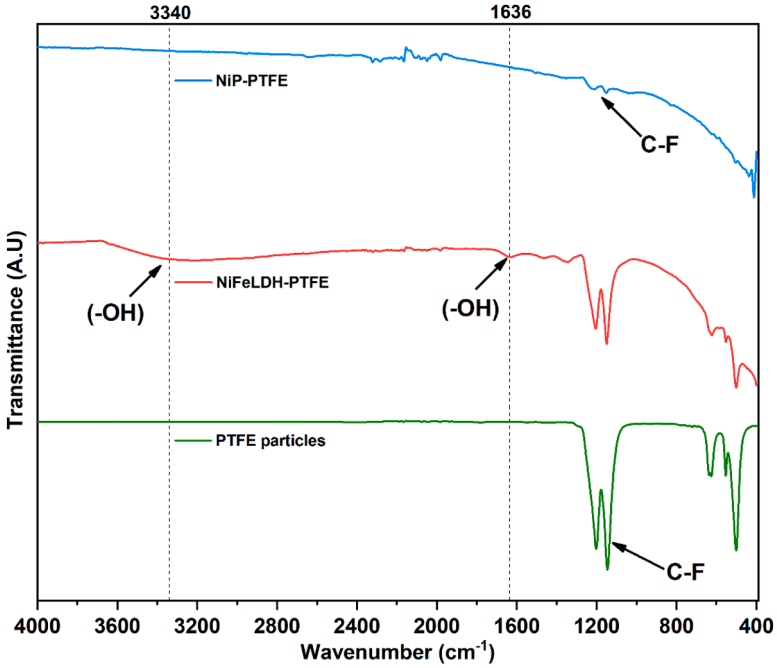

Fig. 2. FT-IR spectra obtained for the different NiP-PTFE and NiFeLDH-PTFE coatings.

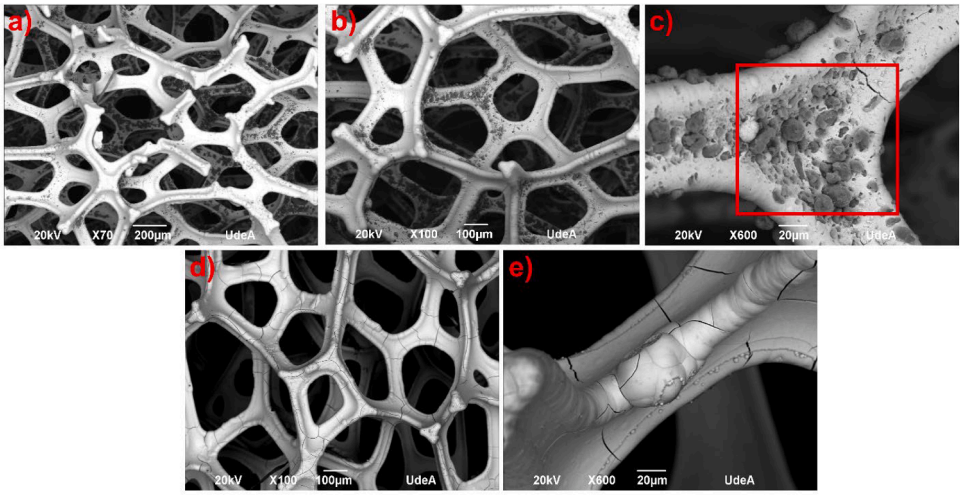

Fig. 3. SEM image of NiP coated samples obtained from electrolytic baths at 450 rpm of stirring speed. (a-c) NiP-PTFE; PTFE-rich agglomerates/nodules are highlighted with red rectangles. (d-e) NiP without PTFE.

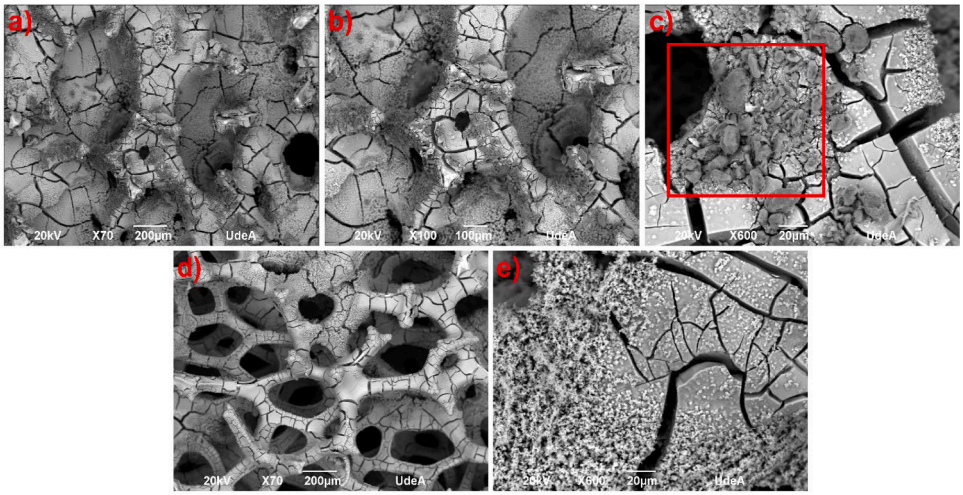

Fig. 4. SEM image of NiFeLDH coated samples obtained from electrolytic baths at 300 rpm of stirring speed. (a-c) NiFeLDH-PTFE; PTFE-rich agglomerates/nodules are highlighted with red rectangles. (d-e) NiFeLDH without PTFE.

particle surface [32,51]. The positive charge facilitates stronger attraction of the particles to the electrode surface, which ultimately increases the number of deposited particles [31] The electrochemical growth of the Ni or NiFe deposit traps the particle clusters on the surface [18]. Figs. S4 and S5, in the supporting information, show SEM images of NiFeLDH-PTFE and NiP-PTFE coatings obtained at 450 rpm, 200 rpm, 600 rpm and 300 rpm of the bath, respectively. This was done to compare the co-deposition of PTFE at different agitation speeds of the electrolytic bath. Regarding the co-deposition of the dispersed phases, the coatings tend to form particle agglomeration, resulting in a heterogenous composite structure where the metal matrix traps PTFE particles. In turn, the electrolyte reaches the edges and internal pores of the nickel foam, resulting in an integrated coating forming in the Ni foam. Nonetheless, the coating morphology was influenced by the co-deposition of PTFE nodules and the presence of Fe and P for each coating produced. Depending on the coating, PTFE nodules were co-deposited on various Ni or NiFe nodules or plates. The PTFE deposits are present in micrometer clusters dispersed throughout most pores of the Ni foams. Additionally, the co-deposition of PTFE, due to its nature and properties, tends to increase the roughness of the coating. This is caused by the dispersion of phases in the electrolytic bath, which promotes the growth of rough deposits because non-conductive PTFE particles are trapped by the conductive metal matrix coatings [52]. The roughness generated on the electrodeposited PTFE containing-coatings is expected to have a positive effect on the formation of larger electrochemically active areas due to the increase in surface area that can occur because of the incorporation of PTFE particles, as will be described in the following sections. Fig. 3 and Fig. 4 confirm that the PTFE particles in the electrodeposited coating are heterogeneously distributed over the surface, which can be called "hydrophobic mosaic" [12]. These can help to reduce the overpotentials of the reactions involved (HER and OER) since these hydrophobic islands can act as gas nucleation points that help generate small bubbles on these "islands" rather than on the catalytic surfaces of the electrode [12]. In other words, the role of incorporated PTFE particles is to create discrete points of the surface where bubbles preferentially nucleate and release, leaving the catalytic part of the coating free or only partially covered by some generated bubbles.

Fig. S7 and S8, in the supporting information, show EDS mapping of the NiFeLDH-PTFE and NiP-PTFE samples, respectively, obtained at stirring speeds in the electrolytic bath of 300 rpm and 450 rpm, respectively. The images show an almost homogeneous distribution of disperse phases on the surface samples and seemingly large PTFE content (see the carbon content in the images) in the sample obtained at low stirring speed. The concentration of PTFE on the coating largely depends

on the stirring of the electrolytic bath, as has been mentioned in literature reports [53,54].

Figures S8 ((a)-(d)) in the supplementary information present the thermograms obtained by TGA under a nitrogen atmosphere for NiFeLDH and NiP samples containing PTFE. The thermogravimetric analysis of the NiFe-LDH and NiP materials reveals distinct thermal behaviors related to their chemical structure and composition, demonstrating mass loss events consistent with the contact angle and morphological (SEM) results. For NiFeLDH-PTFE coatings (Figure S8 (a) and (b)) synthesized at 900 rpm and 300 rpm, three main stages of mass loss were identified under a nitrogen atmosphere. The first stage, occurring below 180 °C, corresponds to the removal of adsorbed moisture. The second stage, between 180 °C and 350 °C, is associated with the decomposition of intercalated anions (such as NO_3^- and OH^-) and interlayer water [55,56]. Finally, a third stage is observed in PTFE-containing coatings, characterized by a two-step thermal degradation mechanism related to the decomposition of the polymeric fraction (PTFE) in both formulations. According to the literature, the first step, occurring at 508.2 °C, corresponds to a first-order kinetic mechanism that generates free radicals at the ends of the polymer chains. The second step, at 570.4 °C, involves the reaction between these free radicals and macromolecules, leading to the formation of tetrafluoroethylene (C_2F_4), a volatile compound [57,58]. In contrast, the NiP-PTFE coatings (Figure S8 (c) and (d)) exhibit no significant mass loss related to oxide formation in the range of 25 to 450 °C, highlighting their excellent thermal stability. However, similarly to NiFe-LDH-PTFE coatings, significant mass losses were observed in the 500–650 °C temperature range, albeit to a lesser extent, which are attributed to the degradation mechanism and volatile PTFE compounds previously described. For NiFeLDH-PTFE coatings, mass losses of 16.59 ± 0.84 % and 10.94 ± 0.36 % were recorded at 300 RPM and 1200 RPM, respectively, attributed to the thermal degradation of the PTFE polymer in the coating. In the case of NiP-PTFE, the mass losses were lower than those mentioned above, ranging from 5.53 ± 0.65 % to 3.85 ± 0.39 % at stirring speeds of 450 RPM and 900 RPM, respectively, also associated with the presence of PTFE. This analysis confirms that coatings produced at lower stirring speeds (300 rpm for NiFeLDH-PTFE and 450 rpm for NiP-PTFE) in electrochemical baths favor higher PTFE co-deposition.

3.3. Electrochemical characterization of catalytic coatings

LSV, CV, and durability tests were performed during the alkaline water electrolysis process on samples coated with the optimal PTFE concentration (30 g L^{-1}). Fig. 5 shows the LSV curves recorded at a scan rate of 5 mV s^{-1} in 1 M NaOH for coatings obtained at different stirring speeds of the electrolyte bath. LSV curves for the OER are shown in Figure 5(a) show a clear improvement in performance at industrially relevant current densities. At 100 mA cm^{-2}, the overpotential decreases by ~20 mV compared to the PTFE-free electrode when the stirring rate during synthesis is reduced to 300 rpm. This improvement is attributed to the higher PTFE incorporation into the coating as agitation is lowered (see TGA results). Such a reduction is significant in terms of cell-voltage savings and is consistent with enhanced gas management and/or an increased effective electrochemically active area under vigorous gas evolution conditions [59].

The dependence on stirring speed can be rationalized by

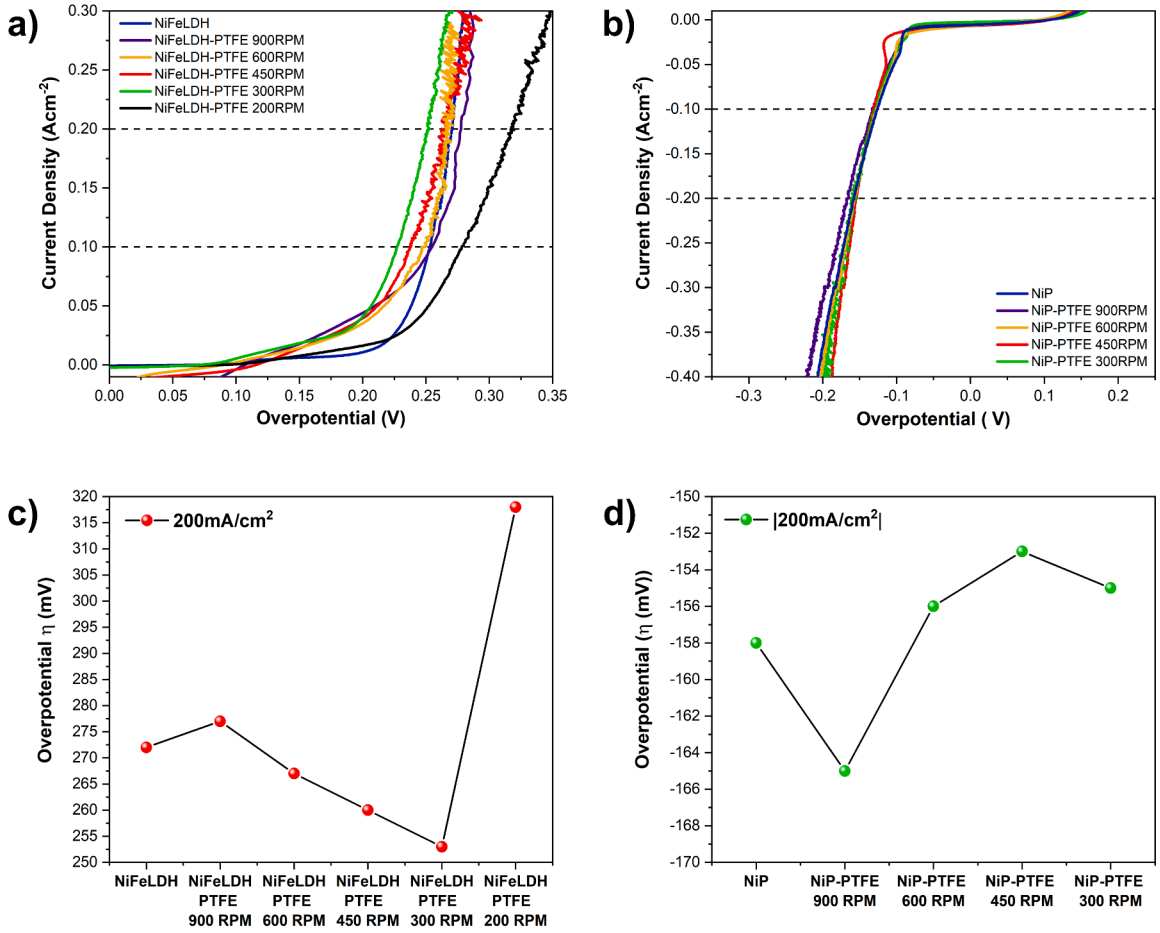

Fig. 5. LSV curves at a scan rate of 5 mVs^{-1} in 1 M NaOH unstirred electrolyte a) OER and b) HER. Variation of anodic and cathodic overpotentials at |200 mA cm^{-2}| at different stirring rates for c) NiFeLDH-PTFE coating and d) NiP-PTFE coating.

hydrodynamic effects on PTFE particle transport and entrapment during composite codeposition [33,60] . At high stirring rates during synthesis, strong shear and short particle residence times near the electrode surface can hinder particle adsorption/retention and reduce PTFE incorporation, thereby weakening the intended hydrophobic mosaic and diminishing bubble-release efficiencyIn contrast, moderate stirring (300 rpm) balances particle suspension and residence time, promoting uniform incorporation and improved bubble detachment. At lower stirring rates (200 rpm), performance deteriorates, likely due to insufficient suspension and mass transport, which can lead to PTFE agglomeration and non-uniform deposition, hindering the formation of an effective surface for bubble removal.

Quantitatively, the OER overpotentials at 100 mA cm^{-2} were 255, 247, 238, 227, and 278 mV for NiFeLDH coatings with PTFE at stirring speeds of 900, 600, 450, 300, and 200 rpm, respectively, while the PTFE-free NiFeLDH exhibited 250 mV. Overall, stirring speed has a limited effect on intrinsic catalytic activity; however, its influence becomes more evident at high current densities, where bubble accumulation and interfacial transport limitations significantly affect the measured overpotential [61]. In this context, PTFE incorporation improves OER performance by facilitating bubble release and reducing anodic overpotential, particularly under intense gas evolution conditions (Fig. 5c).

The HER LSV curves are shown in Fig. 5b At 100 mA cm^{-2}, the NiP coatings with PTFE exhibit overpotentials of 131, 127, 130, and 128 mV for stirring speeds of 900, 600, 450, and 300 rpm, respectively, compared to 125 mV for the PTFE-free NiP coating. These similar values indicate that PTFE has a negligible effect on HER overpotential under dynamic conditions and at relatively low current densities. However, at higher current densities (−200 mA cm^{-2}), a reduction in overpotential becomes more evident (Fig. 5d), likely due to increased H_2 bubble generation. The role of PTFE in bubble management is further discussed based on long-term stationary measurements.

Coated samples were evaluated under steady-state conditions by chronopotentiometry. NiFeLDH-PTFE and NiP-PTFE coatings samples were tested for 5 h of polarization at |400| mA/cm^2 for alkaline water splitting in unstirred 1 M NaOH providing a consistent operating environment. The corresponding curves for samples prepared at different stirring speeds (200–900 rpm) are shown in Fig. S9(a–b). For the NiFeLDH-PTFE coating evaluated under anodic conditions, the OER overpotentials tend to decrease as the stirring speed of the electrochemical bath is reduced. When the stirring speed was reduced, a decrease in the overpotential was observed for the coatings with PTFE, reaching values between 0.27 and 0.275 V at 300 rpm. Again, further reduction in stirring speed to 200 rpm has opposite result and the overpotential increases. For the base material without PTFE the overpotential obtained was approximately 0.3 V. All coatings evaluated at OER conditions showed good stability over 5 h of oxygen evolution. The effect of stirring during electrodeposition is significant as it helps to achieve more homogeneous coating and facilitates electrolyte renewal. This method is described as optimal for incorporating significant concentrations of dispersed phases in different types of coatings. In addition, periodic stirring allows the particles to remain suspended in the solution and settle on the cathode as the process progresses [62].

Similar trends were observed for HER, see Figure S9(b) in the supporting information. The NiP-PTFE coatings prepared at different stirring speeds (300, 450, 600, and 900 rpm) show that, when stirring speed is reduced until reaching 450 rpm the HER cathodic overpotential decreases, after which the cathodic performance deteriorates. However, it remains superior to the base material (without PTFE). For the NiP-PTFE coating prepared at 450 rpm the lowest overpotential was obtained, which was approximately between −0.19 V and −0.195 V at a current density of |400| mA cm^{-2}. This represents a lower overpotential than that reported by other authors for NiP without PTFE [63]. Based on these results, the NiFeLDH-PTFE electrodes obtained with a concentration of 30 g L^{-1} of PTFE and stirring of 300 rpm and NiP-PTFE with stirring of 450 rpm were selected as the optimal for further tests of OER and HER, respectively.

The high electroactivity of HER and OER observed in NiFeLDH-PTFE and NiP-PTFE electrodes can be attributed to advantages such as the three-dimensional porous structure and the limited wettability of the electrodes due to PTFE incorporation. This is an interesting issue that could be controversial, because the wettability of the catalysts is particularly important in electrochemical reaction processes, as good wettability favors the dissociation of H—OH on the electrode surfaces [63]. On the other hand, aerophilic surfaces favor the release of gases and reduce ohmic loss during gas evolution.

In this context, PTFE incorporation creates a heterogeneous surface with localized hydrophobic domains, which promotes gas release while maintaining sufficient electrolyte contact. Previous studies have shown that PTFE-containing electrocatalysts can enhance the removal, coalescence, and transport of gas bubbles during operation [11,28,54]. Due to its low surface energy and aerophilic nature, PTFE is likely to improved performance by reducing bubble accumulation at both the anode and cathode. Additionally, the increased surface roughness associated with PTFE incorporation may facilitate bubble migration along the gas–liquid interface, further enhancing mass transport, thus preventing bubble accumulation and formation [54].

In addition, as observed in the steady-state tests, PTFE could indirectly improve the catalytic performance of the electrodes, due to its effect on the physical and structural properties of the coating, rather than by directing affectation of the intrinsic catalytic activity. This optimization allowed for better bubble release, increased the active area, and improved the stability of the coating during HER and OER reactions. Furthermore, Figure S9 shows that increased PTFE deposition also helps to reduce overpotential by preventing the blocking of the active area of the electrode. This finding is consistent with the previously presented TGA results, which showed that lower stirring speeds allowed more PTFE to be co-deposited in the respective coatings.

To further evaluate the electrochemically active surface area, cyclic voltammetry (CV) measurements were performed at different scan rates for NiP and NiFeLDH coatings, with and without PTFE, prepared under optimal stirring conditions (450 rpm for NiP and 300 rpm for NiFeLDH). Measurements were conducted in a non-Faradaic potential region near the open circuit potential (±0.1 V for NiP and ±0.05 V for NiFeLDH), allowing the capacitive response to be isolated (see Figs. S9 and S10).

Figs. 6 and 7 shows plots of current density (A/cm^2) as a function of scan rate (mV/s) for NiP and NiFeLDH electrocatalytic coatings, respectively. All plots clearly show linear behavior. From the linear relationship, the differential capacitance (C_d) is obtained according to Eq. (5). This linear slope is interpreted as the capacitive area of the electrode [64]. The capacitance values obtained from the CV measurements are shown in Table 2. The results show a significant variation in the NiFeLDH and NiFeLDH-PTFE coatings, with a fivefold increase from 0.42 mF cm^{-2} without PTFE to 1.96 mF cm^{-2} with PTFE. For NiP and NiP-PTFE, the capacitance increases tenfold from 2.65 mF cm^{-2} to 28.2 mF cm^{-2}. Table 2 also includes the area factor or roughness factor (Rf), which is related to the ECSA of the electrodes. This factor is defined as the ratio between C_d and the reference capacitance (C_{ref}), which corresponds to the capacitance of an electrode with an ideally flat surface, according to Eq. (6) [65]. In this case, a reference capacitance of C_{ref} = 40 μF cm^{-2} was used, as reported in the literature [66].

$$J_C = C_D \nu \tag{5}$$

$$R_{AC} = \frac{Cd}{Cref} \tag{6}$$

Based on the SEM observations and the calculated Rf, the incorporation of PTFE leads to a moderate increase in the electrochemically active surface area. This enhancement can be attributed to the development of surface heterogeneities and interconnected porosity arising from the co-deposition of PTFE particles. Consequently, the improved

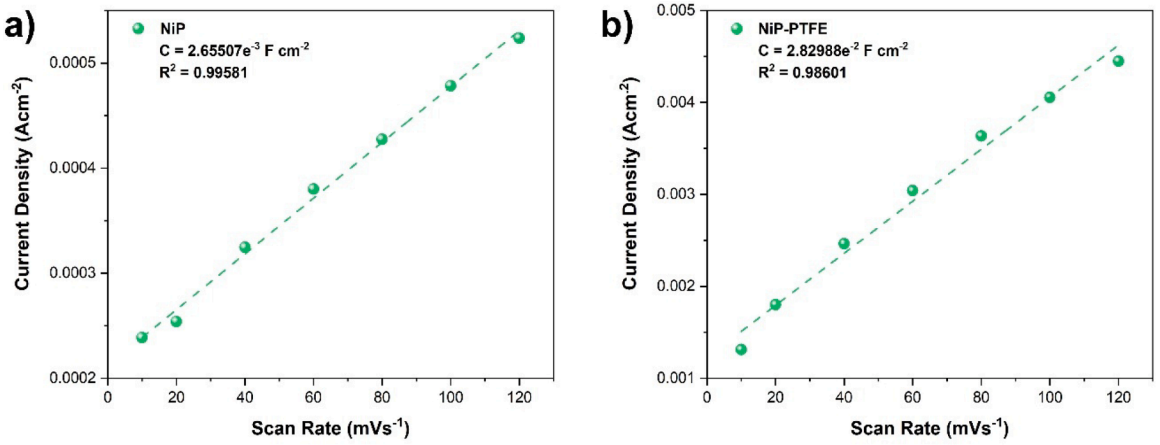

Fig. 6. Current density vs. scan rate curves obtained from CV curves (Fig. S10). a) NiP, b) NiP-PTFE.

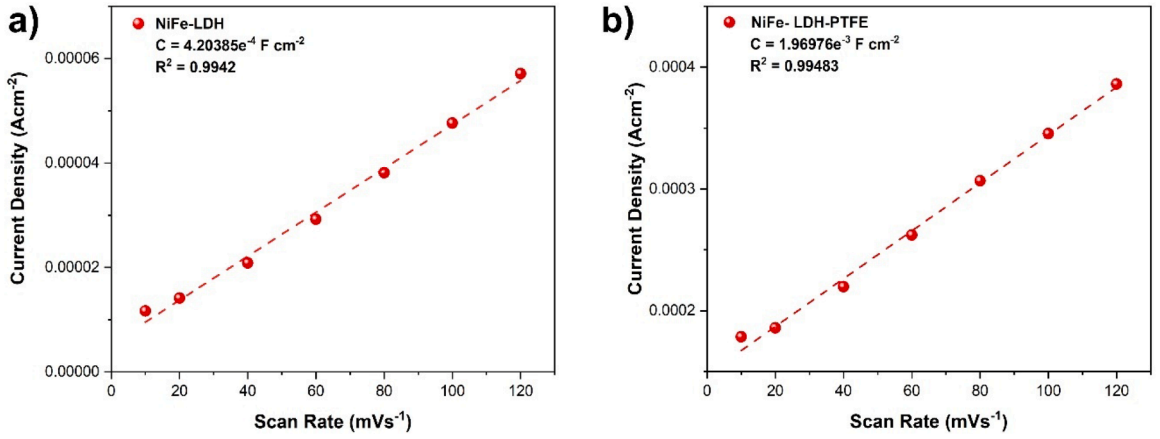

Fig. 7. Current density vs. scan rate curves obtained from CV curves (Fig. S11). a) NiFeLDH, b) NiFeLDH-PTFE.

Table 2
Calculated parameters from CV curves of different electrodes.

Coating	Cd (F/cm^2)	R_f
NiFeLDH	4.20385×10^{-4}	10.50
NiFeLDH-PTFE	1.96603×10^{-3}	49.15
NiP	2.65507×10^{-3}	66.37
NiP-PTFE	2.82988×10^{-2}	707.47

performance of PTFE-containing electrodes can be associated with an increase in surface roughness and the formation of a more irregular and heterogeneous topography. This interpretation is consistent with the work of Hodges et al. [28], who reported a significant increase in capacitance upon PTFE incorporation, linked to enhanced porosity and electrochemically active surface area.

Notably, as is shown in Table 2, the Rf value observed for NiP- PTFE is approximately 14 times larger than NiFeLDH- PTFE. This result is mainly attributed to differences in the morphology of the catalytic coating's base layer, as was evidenced by the SEM images, see Figs. 3 and 4 and Figure S3, in the supporting information. Specifically, NiFeLDH base layer exhibits a layered platelet-like structure with surface oxides, whereas NiP forms a more compact and nodular coating morphology. The morphological differences influence the way PTFE is incorporated into each material. In the case of NiP, the compact structure promotes a more effective interaction with PTFE, leading to a more pronounced increase in surface roughness and electrochemically active area. In contrast, the layered structure of NiFeLDH may limit the accessibility and distribution of PTFE within the coating, resulting in a smaller increase in Rf. Furthermore, the greater performance enhancement observed under steady-state conditions suggests that PTFE incorporation not only increases the electrochemically active surface area but also facilitates bubble detachment, thereby improving mass transport during operation.

The stability test of the optimal coatings prepared with 30 g L^{-1} PTFE and the best stirring speeds in the electrochemical baths of 300 rpm for NiFeLDH-PTFE and 450 rpm for NiP-PTFE, are shown in Fig. 8 for electrodes with and without PTFE, at a current density of |400| mA cm^{-2}. The performance of the electrodes remained stable throughout the evaluation period. This indicates that the integrated NiFeLDH-PTFE and NiP-PTFE electrodes have good electrochemical stability with no detectable degradation over 24 h. This result confirms the excellent catalytic stability of NiFeLDH-PTFE for OER and NiP-PTFE for HER. Small potential fluctuations were observed, usually attributed to the adsorption/desorption of oxygen and hydrogen bubbles on the electrode surface. In addition, it is shown that the incorporation of PTFE particles results in lower overpotentials even during longer tests, decreasing from an overpotential range of 275–280 mV for NiFeLDH to a range of 228–233 mV for NiFeLDH-PTFE. NiP overpotentials range from 225 to 235 mV, slightly higher than NiP-PTFE overpotentials, which range from 190 to 195 mV.

The increase in overpotential in the base layer and the observed oscillations could be related to the continuous accumulation of bubbles mentioned above. These bubbles accumulate on the electrode surface, causing ohmic losses due to the increasing resistance and reduction of

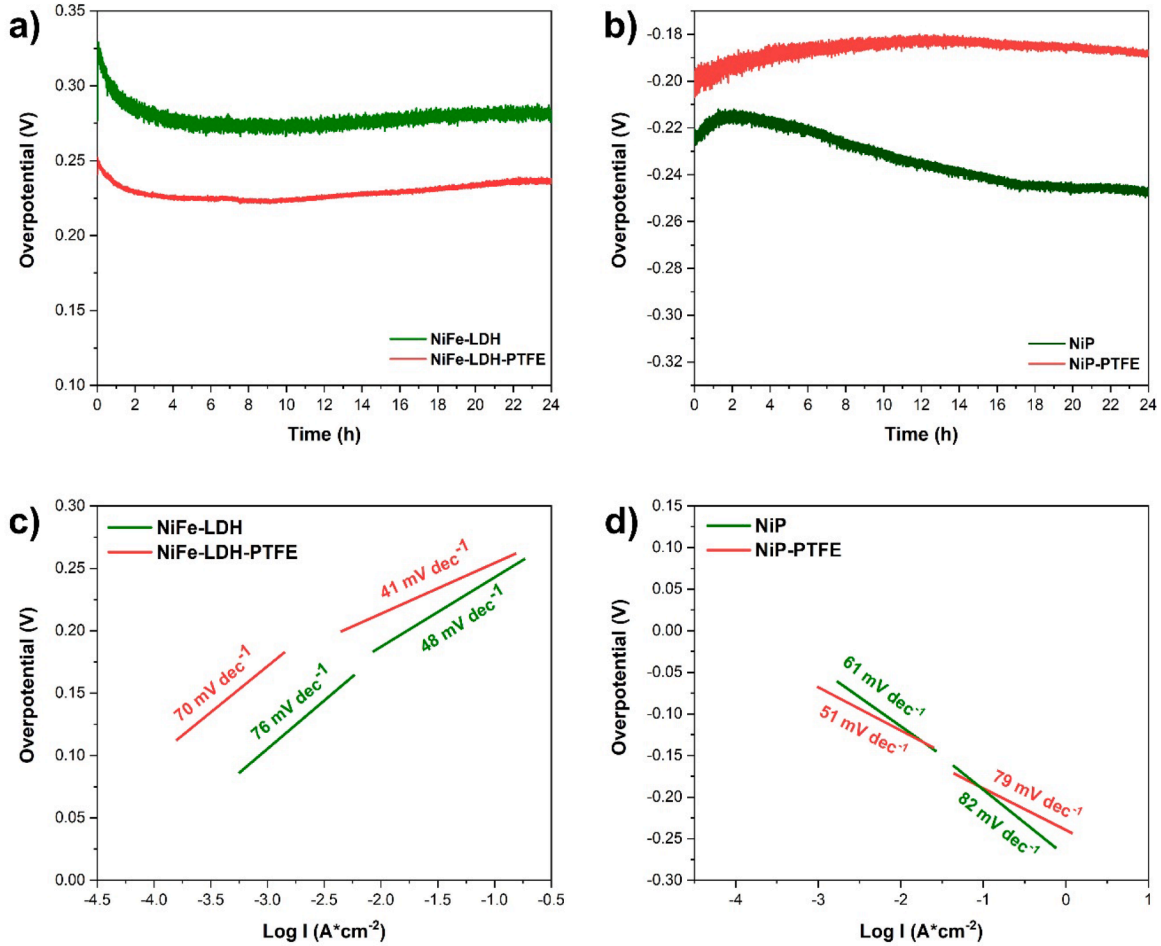

Fig. 8. Catalytic stability of the electrodes analyzed from chronopotentiometry curves of the samples at |400| $mAcm^{-2}$ in an unstirred electrolyte of 1 M NaOH and Tafel slopes for the different coating systems. a) Anodic chronopotentiometry (OER), b) Cathodic chronopotentiometry (HER), c) Anodic Tafel slope (OER), and d) Cathodic Tafel slope (HER).

the electrochemical-active area, which is blocked by the bubbles produced during the reactions. This prevents the interaction between the catalytic surface and the electrolyte. In contrast, nucleation and growth of bubbles occurs preferentially at the PTFE-catalyst interface due to the high surface energy of those sites. So, due to the hydrophobicity of that interface, the bubble release is facilitated. The gases formed due to the reactions involved in the process may have a hydrophobic nature, causing them to accumulate at preferred sites on PTFE-coated surfaces selectively [18,67]. For example, electrodes made of Ni sheets with selective PTFE islands on the surface generate bubbles primarily on the PTFE islands rather than on the Ni at low voltages during water electrolysis [68] The smaller number of bubbles blocking the ECSA may be due to the preferential coalescence of the newly formed gas on the PTFE surface.

Beyond the presence of PTFE within the electrodes, the long-term trend observed in Fig. 8a suggests an activation process rather than merely stable operation, as the overpotential progressively decreases with time. A plausible explanation is the gradual incorporation of Fe into the Ni-based (oxy)hydroxide surface under anodic polarization, leading to the formation of Ni(Fe)OOH-like active sites with enhanced OER kinetics. This effect is well documented: even trace levels of Fe in alkaline electrolytes can be incorporated into $Ni(OH)_2$/NiOOH, markedly boosting OER activity by increasing the intrinsic activity of the active site and/or by modifying the redox chemistry of the catalytically active phase [69,70] . In contrast, the time-dependent behavior in Fig. 8b indicates that additional processes beyond intrinsic catalytic kinetics may govern the long-term response. Accordingly, a gradual increase in overpotential (or a time-dependent change in slope) may be rationalized by a progressive loss of effective active area and/or increased bubble adhesion/retention, potentially associated with changes in surface wettability (e.g., PTFE redistribution, partial detachment, pore blockage, or flooding of the porous structure). Such bubble-induced limitations are known to become more pronounced at extended times and at high current densities [61,71].

Overall, PTFE incorporation improves performance by enhancing bubble management and maintaining the accessibility of catalytic sites, resulting in a reduction of 30–40 mV in overpotential at 400 mA cm^{-2} compared to PTFE-free coatings. This improvement is attributed to more efficient utilization of the electrochemically active surface area.

The LSV curves were also recorded before and after the long-term durability tests, as shown in Figure S12. At low current densities (|30| mA cm^{-2}), very similar performance of the coatings was observed before and after the tests. However, at high current densities (above |100| mA cm^{-2}), a significantly lower overpotential was observed in the coatings after the test for both catalysts with and without PTFE, confirming the stability and durability of the catalysts in HER and OER operation under alkaline conditions. The overpotential values obtained before and after the durability tests are given in Table S1 in the supporting information. These results also confirm that the presence of hydrophobic PTFE particles in the coating does not negatively affect the catalytic performance of the electrode. On the contrary, the good catalytic performance of the coatings is maintained or even improved by the hydrophobicity of the PTFE particles, especially at high current densities where bubble formation is enhanced. In addition, the morphology of NiFeLDH with and

without PTFE remained in good condition after 24 h of OER operation at |400| mA cm^{-2}, without significant changes (Figure S13). Similarly, the morphology of NiP with and without PTFE was preserved after the HER stability tests (Figure S14).

The anodic and cathodic Tafel slopes for the OER and HER, obtained from potentiodynamic polarization in 1.0 M NaOH electrolyte at a scan rate of 80 μV s^{-1}, are shown in Figs. 8(c) and (d), respectively. Two distinct Tafel slope regions were identified for all developed coatings, both with and without PTFE: one corresponding to low overpotentials and another to high overpotentials. This variation in the polarization curve slopes suggests the occurrence of two different electrochemical mechanisms, likely associated with the formation of distinct intermediate species and differences in the rate-limiting steps that govern the reaction during anodic polarization in each overpotential range. These observations support the good catalytic behavior of the developed coatings [72]. The Tafel slope values obtained at high and low overpotentials for the respective coatings are also shown in Fig. 8c-d. Overall, the PTFE-containing coatings exhibit slightly lower Tafel slopes compared to the PTFE-free samples. This indicates a modest improvement in apparent kinetics, which can be attributed primarily to reduced surface blockage by gas bubbles. The cathodic Tafel slopes suggest favorable kinetics for the HER. This is because the composite structure enhances the interaction of water molecules with the catalyst surface, thus accelerating the formation of hydrogen adsorption intermediates [73,74]. The above indicates that the NiP systems evaluated in this work are governed by a mixed Volmer-Heyrovsky mechanism. A similar behavior was observed for OER, demonstrating a high catalytic activity for water splitting for the electrodeposited catalysts [75]. In summary, a slight reduction of the Tafel slopes for water splitting was observed when PTFE particles are incorporated into the catalytic coatings, indicating that reaction mechanisms and kinetics do not change appreciably because of the presence of PTFE. Conversely, a slight improvement in kinetics may occur due to the increase in the ECSA, see Table 2, which was observed when PTFE particles are present in the catalytic coating.

Figs. 9 and 10(a) - (c) show the Nyquist and Bode plots of the electrochemical impedance obtained for the coatings at anodic and cathodic polarization potentials (0.564 V vs. Hg/HgO) and (−1.130 V vs. Hg/HgO), respectively. The Nyquist plots from the EIS measurements of the anodic OER reaction show the presence of at least two time-constants (two coupled capacitive loops) at high and intermediate frequencies, constitutive of the anodic process, and a third time-constant at low frequencies presented only in samples with PTFE, related to the PTFE interface. The presence of these three time-constants is more evident in the Bode-Phase plots, Fig. 9c. The capacitive loop at high frequencies is related to the charge-transfer resistance of the OER in parallel with the double-layer capacitance. Meanwhile the second capacitive loop at low frequencies could be related to the surface reaction of the electrode material, such as oxidation and structure transformations, as has been observed in previous works [35,76,77]. Therefore, the electrocatalytic activity of the coating surface can be followed through the changes in the charge-transfer resistance of the first capacitive loop. The EIS results were fitted with the equivalent electrical circuits (EEC) shown in Fig. S15 in the supporting information, and the electrical parameters of the EIS results are presented in Table S2. The charge-transfer resistance for OER of the NiFeLDH-PTFE coating ($\mathbf{R_{t1}}$=0.102 ohm) is lower than that of the NiFeLDH without PTFE ($\mathbf{R_{t1}}$=0.356 ohm), indicating faster and more kinetically favorable OER on the NiFeLDH-PTFE coating than on the NiFeLDH coating. Similarly, the resistance of the second time-constant ($\mathbf{R_{t2}}$) of the NiFeLDH-PTFE coating is lower than that of the NiFeLDH without PTFE. The presence of PTFE improves the kinetics of OER due to the increase of the ECSA and to better bubble management during gas evolution, as will be further discussed. These results are consistent with the previously mentioned LSV and Tafel polarization results. As expected, the resistance of the third capacitive loop observed only in the coating with PTFE is the largest one, because of the non-conductive character of the PTFE particles.

The Nyquist plots from the cathodic EIS measurements of the NiP and NiP-PTFE coatings for HER reaction are shown in Fig. 10a. Similarly to anodic EIS measurements, cathodic Nyquist plots are constituted by at least two couple time-constants (two coupled capacitive loops) at high and intermediate frequencies, constitutive of the cathodic process, and a third time-constant at low frequencies presented only in the samples with PTFE, related to the PTFE interface. The capacitive loop at high frequencies is related to the charge-transfer resistance of the HER in parallel with the double-layer capacitance. The second capacitive loop at low frequencies could be related to the surface reaction of the electrode material. The parameter's fit of EIS using an EEC is shown in Table S2. As previously mentioned for anodic EIS measurements, the electrocatalytic activity for HER of the coating surface can be followed through the changes in the charge-transfer resistance of the first capacitive loop. The charge-transfer resistance for HER of the NiP-PTFE coating (R_{t1}=0.1 ohm) is lower than that of the NiP without PTFE (R_{t1}=0.13 ohm), indicating faster and more kinetically favorable HER on the NiP-PTFE coating than on the NiP coating. Similarly to what is mentioned in the anodic analysis, the low value of the charge-transfer resistance for HER is due to the increase in the ECSA and to the better bubble management during H_2 evolution that occurred when PTFE particles are present in the coating. Regarding the Bode plots of EIS spectra, Figs. 9c and 10c, the maximum phase angle first increases in certain parts but gradually decreases with decreasing frequency for NiP and NiFe-LDH with and without PTFE. This could be attributed to the formation of oxidation by-products of the elements that make up the respective coatings (in this case, Ni and Fe), which tend to form passive layers on the surface.

3.4. Evaluation of developed electrodes with and without PTFE in a "zero gap" full cell for overall alkaline water splitting

Considering the excellent HER and OER performance of the NiP-PTFE, NiP, NiFeLDH, and NiFeLDH-PTFE catalysts, we evaluated their practical application as catalysts in a full-cell to assess the real behavior and performance of the system composed of the optimized catalysts

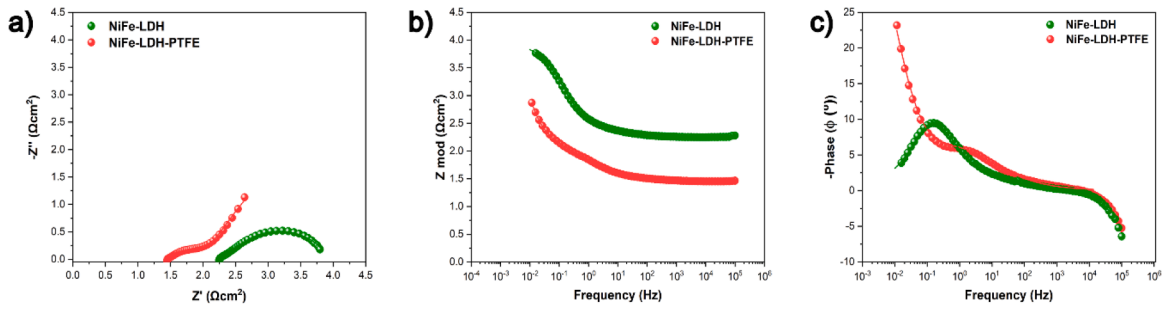

Fig. 9. Electrochemical impedance of the different samples evaluated at anodic potential of 0.564 V vs. Hg/HgO. All measurements were performed in 1 M NaOH. a) Nyquist plot of EIS, b) Bode plot of EIS (|Z| vs Frequency), c) Bode plot of EIS (Φ vs Frequency).

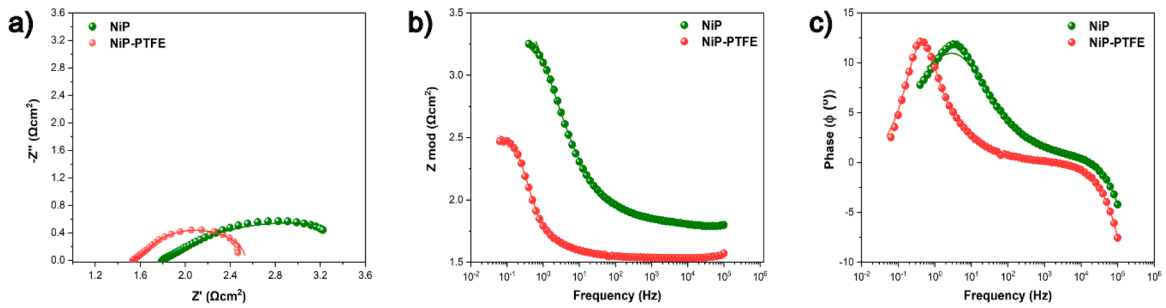

Fig. 10. Electrochemical impedance of the different samples evaluated at cathodic potential of −1.130 V vs. Hg/HgO. All measurements were performed in 1 M NaOH. a) Nyquist plot of EIS, b) Bode plot of EIS (|Z| vs Frequency), c) Bode plot of EIS (Φ vs Frequency).

electrodeposited on Ni foam (NF). We used NiFeLDH coatings with and without PTFE at the anodes and NiP coatings with and without PTFE at the cathodes. The electrolyte consisted of 1 M NaOH solution at room temperature and a separator of PES (Polyether sulfone). LSV curves were recorded at a scan rate of $5mVs^{-1}$. LSV curves performed in full-cell using electrodes with and without PTFE particles for overall alkaline water splitting are shown in Fig. 11. According to the results, the cell containing NiFeLDH-PTFE/NiP-PTFE electrodes displays lower operational potential than the cell containing NiFeLDH/NiP electrodes without PTFE particles. Excellent performance for overall water splitting was observed for the cell containing electrodes with PTFE. The NiFeLDH-PTFE/NiP-PTFE and NiFeLDH/NiP cells display operational potentials of 1.60 V and 1.69 V, respectively, at a current density of 100 mA cm^{-2}. In addition, the improvement of the performance of cells composed of electrodes containing PTFE is more remarkable at high current densities, where bubble generation is accentuated. For example, the cell potential obtained at high current density of 400 mA cm^{-2} were 1.70 V and 1.81 V for NiFeLDH-PTFE/NiP-PTFE and NiFeLDH/NiP, respectively, showing the beneficial effect of PTFE incorporation in the electrodes. The remarkable difference in the cells' performance observed in the LSV curves was also due to the use of a full-cell with zero-gap configuration, see Fig S16, in which the effect of bubbles production and release becomes more important than in a beaker test. The operational potential values were corrected with the ohmic resistance. The comparison of the electrochemical performance at |100 $mAcm^{-2}$| of the developed NiFeLDH-PTFE/NiP-PTFE full-cell compared to other works reported in the literature is presented in Table 3. As can be seen, the developed full-cell electrodes containing PTFE particles are remarkable superior to those reported in other published works.

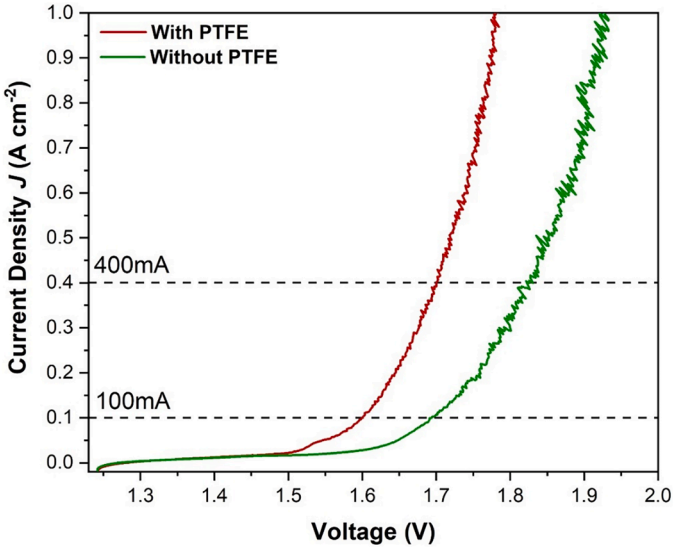

Fig. 11. LSV curves recorded with full cells composed of catalyst coated Ni foam electrodes with and without PTFE for overall water splitting in 1.0 M NaOH. A full cell with PTFE was composed of Ni foam/NiFeLDH-PTFE as anode and Ni foam/NiP-PTFE as cathode. Full cells without PTFE were composed of Ni foam/NiFeLDH as anode and Ni foam/NiP as cathode.

To evaluate the bubble management during water splitting using catalyst-coated Ni foam electrodes with and without PTFE, electrolysis experiments were carried out in a three-electrode cell, where bubble nucleation, growth and detachment from working electrode surface can be observed. Hydrogen and oxygen evolution were studied in a 1 M NaOH solution at room temperature with a current density of ±50 mA/cm^2. The working electrode area was 1.0 cm^2. Video and images were recorded using a mobile device integrated with a 60x microscope. The size of H_2 and O_2 bubbles released from the electrode surfaces during the water electrolysis process was measured by focusing on the bubbles accurately captured by the camera lens. The measurement was performed using the Feret diameter with the *Image J program*. Table 4 shows the measured diameters of the bubbles during the hydrogen and oxygen evolution reactions for the electrodes with and without PTFE.

First all, it was observed that the release of bubbles from the hydrophobic islands of PTFE and other sites on the surface was relatively random. Also, the diameter of the bubbles that detach from the surface and the growth time were not the same for each bubble. From this experimental observation and in conjunction with SEM images, it was found that the surface of the hydrophobic islands was not entirely covered by the PTFE particles, which could be one of the reasons for the differences in bubble size. As can be seen in Table 4, there is a clear tendency to produce larger bubbles when the catalytic coating contains PTFE; the size of the bubbles generated on the PTFE-containing coatings was nearly 50 % larger than the size of the bubbles produced in the coatings without PTFE. This result is related to a decrease in the wettability of the working electrode surface when PTFE particles are present in the catalytic coatings. As was mentioned during the contact angle and hydrophobicity analysis (Section 3.1.) the work of adhesion of the solid-liquid interface is lower in the coatings containing PTFE, meaning that water islands can be easily moved by nascent gas bubbes,

Table 3
Comparison of whole-cell overpotentials obtained at |100 $mAcm^{-2}$| between coatings found in previous work in the literature and the coatings of the present work.

Potential (V)				
	J (mA cm^{-2})		Substrate	Reference
Electrodes	**100**			
NiFeLDH/NiP	1.69V	NF		This work
NiFeLDH-PTFE/NiP-PTFE	1.60V	NF		This work
NiFeP/Zn	1.83V	SS		[78]
Ni-P	1.87V	NF		[79]
Ni_2P/NiMoP	1.68V	NF		[80]
Ni-Fe-S	2.00V	NF		[81]
$NiMn_{1.5}PO_4$/NF	1.67V	NF		[82]
Fe-NiP//Fe-NiP	1.75V	NF		[83]

Table 4
Bubble diameters during hydrogen and oxygen evolution reaction for coatings with and without PTFE.

Feret bubble diameter H_2 (mm)		Feret bubble diameter O_2 (mm)	
Material with PTFE	Material without PTFE	Material with PTFE	Material without PTFE
0.150	0.096	0.269	0.180
0.165	0.089	0.282	0.158
0.176	0.084	0.232	0.145
0.177	0.099	0.258	0.181
0.143	0.079	0.244	0.154
0.139	0.084	0.288	0.177
0.135	0.089	0.264	0.134
0.173	0.079	0.262	0.186
0.158	0.099	0.290	0.150
0.145	0.072	0.285	0.176

facilitating the nucleation and growth of bubbles at the interface when OER or HER occur. In addition, the coatings with PTFE tend to have greater roughness than the base coatings, see Table 2, which can also promote the formation of large bubbles [18,54]. Bubbles form at active points on the electrode, and if those points have low surface tension the phase gas is favored and bubbles rapidly nucleate and grow until detachment occurs [84,85]. Consequently, low surface resistance and low polarization occur because bubble management is facilitated. Although the detachment of larger bubbles could, in principle, aggravate local concentration polarization if they temporarily hinder electrolyte renewal near the electrode surface, our results indicate that this effect was not dominant in the present system. Despite the larger bubble size observed for the PTFE-containing coatings, these electrodes showed lower overpotentials under steady-state operation and better overall water-splitting performance. This suggests that the easier coalescence and faster detachment of bubbles, together with the reduced residence time of gas on the catalytic surface, outweighed any possible local mass-transport limitation associated with the larger detached bubbles.

Fig. 12 shows images of bubble formation and growth from the electrodes. Bubbles nucleate and grow on active sites of the electrodes' surface; they then merge to form a sufficiently large bubble until the internal gas pressure is superior to the adhesion forces and completely detach from the electrode. However, tiny bubbles remain on the surface and attempt to detach rapidly. The number of bubbles produced along the surface of the porous electrode is a reliable indicator of the level of gas stripping activity, as a more significant number of bubbles indicates better production of hydrogen or oxygen at the electrode [68]. In addition, the physical properties of the electrode affect both the behavior, and the number of bubbles produced. Rougher electrodes have a larger surface area, providing more nucleation sites and consequently increasing bubble production. A larger ECSA, as confirmed by the previously shown CVs in these electrodes, increases the number of bubble nucleation sites [54,84–86].

When a current of ±50 mA/cm² was applied to the coatings, the bubbles' movements (nucleation, growth and detachment) were slow for both HER and OER. The bubbles were observed to rise, merge with each other, and adhere to the electrode surfaces. However, different vertical displacements were observed, with some bubbles detaching faster than others. The coalescence of smaller bubbles into larger ones allows for easier and faster detachment, thereby preventing the inhibition of active sites on the materials or blocking them for a shorter period. The interconnected pores and channels created by the 3D foam structure, in combination with the PTFE, not only provide a larger ECSA but also allow for more efficient bubble transport and effectively increase the utilization of these catalytic sites by preventing them from being blocked by the generated bubbles.

4. Conclusion

In this work, integrated coatings consisting of a 3D porous structure with NiFeLDH-PTFE and NiP-PTFE were successfully prepared via a co-electrodeposition process to fabricate electrodes for alkaline water

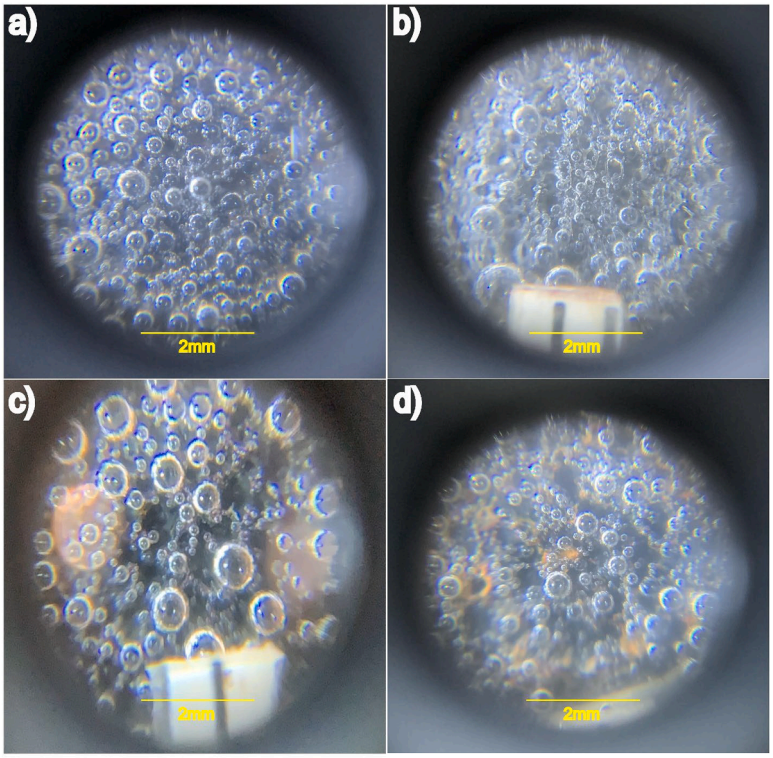

Fig. 12. Images of bubble formation and growth in a gas-filled porous electrode with and without PTFE coating. a) NiP-PTFE, b) NiP, c) NiFeLDH-PTFE, and d) NiFeLDH.

splitting. Their improved catalytic, hydrophobic and protective nature facilitated the highly active surface area of the electrode and optimized surface wettability. Coating electrodes with PTFE improved the performance of water electrolysis cells, especially in stationary conditions. The PTFE coatings exhibited relatively low overpotentials (230 mV and 193 mV for OER and HER, respectively) and good performance in stationary tests at |400| mA/cm^2, compared to the overpotentials shown by the materials without PTFE of 280 mV and 230 mV for OER and HER respectively. Also, they showed good stability throughout the 24 h duration of the test. Finally, full-cell using NiFeLDH/NiP coatings with PTFE showed a very low operating voltage of 1.7 V at 400 mA/cm^2 for overall water splitting. This was a result of several factors, including porous and rough electrode surfaces, high-performance catalytic coatings, surface hydrophobicity, and increased ECSA. Electrochemical investigations showed that, by incorporating PTFE into the surfaces of NiFe-LDH and NiP electrodes, the coatings achieved lower overpotential than surfaces without PTFE. This addition of PTFE particles conferred large hydrophobicity and greater area and roughness on the coatings, which led to low polarization, large stabilities, and overall better electrochemical performance of the electrodes for hydrogen and oxygen evolution reactions. These results demonstrate the promising performance of catalytic coatings of NiP and NiFeLDH with PTFE on the electrodes, which can be used for the construction of alkaline electrolyzers with high energy efficiency and large gas production with low losses.

Associated Content in Supporting Information

Complementary coating characterization: contact angle measurements; Raman spectroscopy; TGA; SEM images for different Ni:Fe ratio, CV curves, LSV curves for 0 and 5 h, SEM images of anodic polarization, EDS spectra, LSV curves for 0 and 24; EDS analysis; fitting results of EIS measurements.

CRediT authorship contribution statement

Juan D. Arias: Writing – original draft, Methodology, Investigation. **Santiago Cartagena:** Writing – review & editing, Methodology, Investigation, Formal analysis, Conceptualization. **Simón Quiroz:** Writing – original draft, Methodology, Investigation, Formal analysis. **Jorge A. Calderón:** Writing – review & editing, Supervision, Project administration, Methodology, Funding acquisition, Conceptualization.

Declaration of competing interest

The authors declare that they have no known competing financial interests or personal relationships that could have appeared to influence the work reported in this paper.

Acknowledgements

The authors would like to thank the Colombian Ministry of Science, Technology, and Innovation, “Minciencias,” by the support provided through the Project 102596 “Desarrollo e implementación de un sistema de almacenamiento y conversión de energía basado en baterías de segundo uso y en la generación de hidrógeno verde” Contract # 112721-392-2023—PERSEO Program.

Supplementary materials

Supplementary material associated with this article can be found, in the online version, at doi:10.1016/j.electacta.2026.148794.

Data availability

Data will be made available on request.

References

[1] W. Yin, L. Yuan, H. Huang, Y. Cai, J. Pan, N. Sun, Q. Zhang, Q. Shu, C. Gu, Z. Zhuang, L. Wang, Strategies to accelerate bubble detachment for efficient hydrogen evolution, Chin. Chem. Lett. 35 (2024) 108351, https://doi.org/10.1016/j.cclet.2023.108351.

[2] N.S. Lewis, D.G. Nocera, Powering the planet: chemical challenges in solar energy utilization, Proc. Natl. Acad. Sci. U.S.A. 103 (43) (2006) 15729–15735, https://doi.org/10.1073/pnas.0710559104.) 10.1073/pnas.0603395103Proc. Natl. Acad. Sci. U. S. A. 104 (2007) 20142.

[3] R. Li, Y. Li, P. Yang, D. Wang, H. Xu, B. Wang, F. Meng, J. Zhang, M. An, Electrodeposition: synthesis of advanced transition metal-based catalyst for hydrogen production via electrolysis of water, J. Energy Chem. 57 (2021) 547–566, https://doi.org/10.1016/j.jechem.2020.08.040.

[4] X. Wang, Y. Zheng, W. Sheng, Z.J. Xu, M. Jaroniec, S.Z. Qiao, Strategies for design of electrocatalysts for hydrogen evolution under alkaline conditions, Mater. Today 36 (2020) 125–138, https://doi.org/10.1016/j.mattod.2019.12.003.

[5] A. Wu, Y. Xie, H. Ma, C. Tian, Y. Gu, H. Yan, X. Zhang, G. Yang, H. Fu, Integrating the active OER and HER components as the heterostructures for the efficient overall water splitting, Nano Energy 44 (2018) 353–363, https://doi.org/10.1016/j.nanoen.2017.11.045.

[6] D. Bae, B. Mei, R. Frydendal, T. Pedersen, B. Seger, O. Hansen, P.C.K. Vesborg, I. Chorkendorff, Back-illuminated Si-based photoanode with nickel cobalt oxide catalytic protection layer, ChemElectroChem 3 (2016) 1546–1552, https://doi.org/10.1002/celc.201500554.

[7] K. Zeng, D. Zhang, Recent progress in alkaline water electrolysis for hydrogen production and applications, Prog. Energy Combust. Sci. 36 (2010) 307–326, https://doi.org/10.1016/j.pecs.2009.11.002.

[8] S.Shiva Kumar, V. Himabindu, Hydrogen production by PEM water electrolysis – a review, Mater. Sci. Energy Technol. 2 (2019) 442–454, https://doi.org/10.1016/j.mset.2019.03.002.

[9] J. Mohammed-Ibrahim, A review on NiFe-based electrocatalysts for efficient alkaline oxygen evolution reaction, J. Power Sources 448 (2020) 227375, https://doi.org/10.1016/j.jpowsour.2019.227375.

[10] M. David, C. Ocampo-Martínez, R. Sánchez-Peña, Advances in alkaline water electrolyzers: a review, J. Energy Storage 23 (2019) 392–403, https://doi.org/10.1016/j.est.2019.03.001.

[11] T. Kou, S. Wang, Y. Li, Perspective on high-rate alkaline water splitting, ACS Mater. Lett. 3 (2021) 224–234, https://doi.org/10.1021/acsmaterialslett.0c00536.

[12] G.F. Swiegers, R.N.L. Terrett, G. Tsekouras, T. Tsuzuki, R.J. Pace, R. Stranger, The prospects of developing a highly energy-efficient water electrolyser by eliminating or mitigating bubble effects, Sustain. Energy Fuels 5 (2021) 1280–1310, https://doi.org/10.1039/d0se01886d.

[13] S. Yuan, C. Zhao, X. Cai, L. An, S. Shen, X. Yan, J. Zhang, Bubble evolution and transport in PEM water electrolysis: mechanism, impact, and management, Prog. Energy Combust. Sci. 96 (2023), https://doi.org/10.1016/j.pecs.2023.101075.

[14] H. Ren, S. Xu, K. Jia, H. Zhou, R.-D. Zhao, D. Zhao, Enhancing water/seawater electrolysis catalysis through Ag doping: high-performance and stable NiCr-LDH for bifunctional electrocatalyst, Surf. Interfaces 78 (2025) 108075, https://doi.org/10.1016/j.surfin.2025.108075.

[15] S. Zhang, Y. Tian, B. Zhang, Y. Pan, Y. Wang, J. Xiang, D. Zhao, R. Zhao, F. Wu, L. Miao, In-situ grown Co0.5Ni0.5Se2@nickel-iron layered double hydroxide heterostructure on nickel foam for high-performance bifunctional electrocatalysis in alkaline and seawater electrolysis, J. Power Sources 667 (2026) 239229, https://doi.org/10.1016/j.jpowsour.2025.239229.

[16] Q. Zhang, H. Zhou, B. Zhang, H. Ren, S. Xu, R.-D. Zhao, F. Wu, L. Miao, Improved bifunctional electrocatalytic water splitting via FeSe/NiP heterostructure for accelerated surface reconstruction, Fuel 410 (2026) 137914, https://doi.org/10.1016/j.fuel.2025.137914.

[17] H. Zhou, R. Li, S. Xu, B. Zhang, R. Zhao, X. Zhao, F. Wu, D. Zhao, Interface Engineering induced homogeneous isomeric bimetallic of CoSe/NiSe$_2$ electrocatalysts for high performance water/seawater splitting, Adv. Sustain. Syst. 9 (2025) 2400849, https://doi.org/10.1002/adsu.202400849.

[18] C. Brussieux, P. Viers, H. Roustan, M. Rakib, Controlled electrochemical gas bubble release from electrodes entirely and partially covered with hydrophobic materials, Electrochim. Acta 56 (2011) 7194–7201, https://doi.org/10.1016/j.electacta.2011.04.104.

[19] Y. He, Y. Cui, Z. Zhao, Y. Chen, W. Shang, P. Tan, Strategies for bubble removal in electrochemical systems, Energy Rev. 2 (2023), https://doi.org/10.1016/j.enrev.2023.100015.

[20] C. Dorrer, J. Rühe, Superaerophobicity: repellence of air bubbles from submerged, surface-engineered silicon substrates, Langmuir 28 (2012) 14968–14973, https://doi.org/10.1021/la303231z.

[21] X. Li, Y. Jiang, Z. Zhang, Z. Jiang, J. Lian, L. Ren, Facile and environmentally-friendly fabrication of underwater superaerophobic and superaerophilic metallic surfaces through laser ablation and heat treatment, Colloids Surf. A Physicochem. Eng. Asp. 621 (2021) 126547, https://doi.org/10.1016/j.colsurfa.2021.126547.

[22] X. Bu, Z. Mao, Y. Bu, Q. Quan, Y. Meng, Z. Lai, D. Chen, P. Xie, H. Li, C. Liu, X. Wang, S.P. Yip, J. Lu, J.C. Ho, Remarkable gas bubble transport driven by capillary pressure in 3D printing-enabled anisotropic structures for efficient hydrogen evolution electrocatalysts, Appl. Catal. B 320 (2023), https://doi.org/10.1016/j.apcatb.2022.121995.

[23] F. Foroughi, C. Immanuel Bernäcker, L. Röntzsch, B.G. Pollet, Understanding the effects of ultrasound (408 kHz) on the hydrogen evolution reaction (HER) and the oxygen evolution reaction (OER) on Raney-Ni in alkaline Media, Ultrason. Sonochem. 84 (2022), https://doi.org/10.1016/j.ultsonch.2022.105979.

[24] H. bo Liu, Q. Hu, L. ming Pan, R. Wu, Y. Liu, D. Zhong, Electrode-normal magnetic field facilitating neighbouring electrochemical bubble release from hydrophobic islets, Electrochim. Acta 306 (2019) 350–359, https://doi.org/10.1016/j.electacta.2019.03.140.

[25] Y. Liu, L. ming Pan, H. Liu, T. Chen, S. Yin, M. Liu, Effects of magnetic field on water electrolysis using foam electrodes, Int. J. Hydrogen Energy 44 (2019) 1352–1358, https://doi.org/10.1016/j.ijhydene.2018.11.103.

[26] H. Matsushima, T. Iida, Y. Fukunaka, A. Bund, W. Plieth, Water electrolysis in a magnetic field, ECS Meeting abstracts MA2006-01 (2006) 890–890. https://doi.org/10.1149/ma2006-01/25/890.

[27] Y. Chen, J. Chen, K. Bai, Z. Xiao, S. Fan, A flow-through electrode for hydrogen production from water splitting by mitigating bubble induced overpotential, J. Power Sources 561 (2023) 232733, https://doi.org/10.1016/j.jpowsour.2023.232733.

[28] A. Hodges, A.L. Hoang, G. Tsekouras, K. Wagner, C.Y. Lee, G.F. Swiegers, G. G. Wallace, A high-performance capillary-fed electrolysis cell promises more cost-competitive renewable hydrogen, Nat. Commun. 13 (2022) 1–11, https://doi.org/10.1038/s41467-022-28953-x.

[29] G. Tsekouras, R. Terrett, Z. Yu, Z. Cheng, G.F. Swiegers, T. Tsuzuki, R. Stranger, R. J. Pace, Insights into the phenomenon of 'bubble-free' electrocatalytic oxygen evolution from water, Sustain. Energy Fuels 5 (2021) 808–819, https://doi.org/10.1039/d0se01633k.

[30] J.J. Borodziński, A. Lasia, Study of hydrogen evolution on selected PTFE-bonded porous electrodes, Int. J. Hydrogen Energy 18 (1993) 985–994, https://doi.org/10.1016/0360-3199(93)90080-T.

[31] D. Iacovetta, J. Tam, U. Erb, synthesis, structure, and properties of superhydrophobic nickel-PTFE nanocomposite coatings made by electrodeposition, Surf. Coat. Technol. 279 (2015) 134–141, https://doi.org/10.1016/j.surfcoat.2015.08.022.

[32] L. Bai, Y. Chen, H. Yin, X. Sui, D. Wu, Y. Feng, Insights into the stability of polytetrafluoroethylene aqueous dispersion: role of surfactant, J. Mol. Liq. 314 (2020) 113662, https://doi.org/10.1016/j.molliq.2020.113662.

[33] A. Lelevic, F.C. Walsh, Electrodeposition of Ni[sbnd]P composite coatings: a review, Surf. Coat. Technol. 378 (2019), https://doi.org/10.1016/j.surfcoat.2019.07.027.

[34] Y.H. You, C.D. Gu, X.L. Wang, J.P. Tu, Electrochemical preparation and characterization of Ni-PTFE composite coatings from a non-aqueous solution without additives, Int. J. Electrochem. Sci. 7 (2012) 12440–12455, https://doi.org/10.1016/s1452-3981(23)16557-6.

[35] S. Cartagena, F.E. Bedoya-Lora, J.A. Calderón, Enhancement of anodically treated stainless steel by NiFeP-catalyst electrodeposition as bifunctional electrodes for water electrolysis, J. Electrochem. Soc. 169 (2022) 044501, https://doi.org/10.1149/1945-7111/ac5ff1.

[36] S. Cartagena, J.A. Calderón, High performance of electrochemically modified-polypropylene electrodes for alkaline water splitting, Electrochim. Acta 407 (2022) 139884, https://doi.org/10.1016/j.electacta.2022.139884.

[37] B. Hirschorn, M.E. Orazem, B. Tribollet, V. Vivier, I. Frateur, M. Musiani, Electrochimica Acta determination of effective capacitance and film thickness from constant-phase-element parameters, Electrochim. Acta 55 (2010) 6218–6227, https://doi.org/10.1016/j.electacta.2009.10.065.

[38] F. Wang, S. Arai, M. Endo, Electrochemical preparation and characterization of nickel/ultra-dispersed PTFE composite films from aqueous solution, Mater. Trans. 45 (2004) 1311–1316, https://doi.org/10.2320/matertrans.45.1311.

[39] L. Isern, S. Impey, H. Almond, S.J. Clouser, J.L. Endrino, PTFE layer formation during brush electroplating of nickel, Sci. Rep. 14 (2024) 24069, https://doi.org/10.1038/s41598-024-71376-5.

[40] D.Y. Kwok, A.W. Neumann, Contact angle interpretation in terms of solid surface tension, Colloids Surf. A Physicochem. Eng. Asp. 161 (2000) 31–48, https://doi.org/10.1016/S0927-7757(99)00323-4.

[41] B.H. Stuart, B.J. Briscoe, A fourier transform Raman spectroscopy study of poly (ether ether ketone)/polytetrafluoroethylene (PEEK/PTFE) blends, Spectrochim. Acta A 50 (1994) 2005–2009, https://doi.org/10.1016/0584-8539(94)80212-2.

[42] S. Schröder, T. Strunskus, S. Rehders, K.K. Gleason, F. Faupel, Tunable polytetrafluoroethylene electret films with extraordinary charge stability synthesized by initiated chemical vapor deposition for organic electronics applications, Sci. Rep. 9 (2019) 1–7, https://doi.org/10.1038/s41598-018-38390-w.

[43] S.P. Firsov, G.R. Zhbankov, M. Bakhramov, A. Abdukadyrov, A. Gafurov, Raman spectra and structure of polytetrafluoroethylene subjected to elastic deformation grinding, J. Appl. Spectrosc. 59 (1993) 644–647, https://doi.org/10.1007/BF00661793.

[44] P.R. Riley, P. Joshi, H. Penchev, J. Narayan, R.J. Narayan, One-step formation of reduced graphene oxide from insulating polymers induced by laser writing method, Crystals (Basel) 11 (2021) 1–17, https://doi.org/10.3390/cryst11111308.

[45] L. Yan, Y. Ren, J. Shen, H. Wang, J. Ning, Y. Zhong, Y. Hu, Visible-light-driven electrocatalytic oxygen evolution reaction: niFe2O4/NiFe–Layered double hydroxide Z-scheme heteronanosheet as a model, Energy Technol. 8 (2020), https://doi.org/10.1002/ente.202000607.

[46] F. Tang, T. Liu, W. Jiang, L. Gan, Windowless thin layer electrochemical raman spectroscopy of Ni-Fe oxide electrocatalysts during oxygen evolution reaction, J. Electroanal. Chem. 871 (2020) 114282, https://doi.org/10.1016/j.jelechem.2020.114282.

[47] J. Qian, Y. Zhang, Z. Chen, Y. Du, B.J. Ni, NiCo layered double hydroxides/NiFe layered double hydroxides composite (NiCo-LDH/NiFe-LDH) towards efficient oxygen evolution in different water matrices, Chemosphere 345 (2023) 140472, https://doi.org/10.1016/j.chemosphere.2023.140472.

[48] K. Yamauchi, Y. Yao, T. Ochiai, M. Sakai, Y. Kubota, G. Yamauchi, Antibacterial activity of hydrophobic composite materials containing a visible-light-sensitive photocatalyst, J. Nanotechnol. (2011) 2011, https://doi.org/10.1155/2011/380979.

[49] J.S.K. Singh, Y.C. Ching, D.S. Liu, K.Y. Ching, S. Razali, S.N. Gan, Effects of PTFE micro-particles on the fiber-matrix interface of polyoxymethylene/glass fiber/polytetrafluoroethylene composites, Materials (Basel) 11 (2018) 1–17, https://doi.org/10.3390/ma11112164.

[50] L. Wan, Z. Xu, B. Wang, Green preparation of highly alkali-resistant PTFE composite membranes for advanced alkaline water electrolysis, Chem. Eng. J. 426 (2021) 131340, https://doi.org/10.1016/j.cej.2021.131340.

[51] V. Shah, B. Bharatiya, A.D. Shukla, T. Mukherjee, D.O. Shah, Adsorption of nonionic Brij and Tween surfactants at PTFE-water and air-water interfaces: investigations on wetting, dispersion stability, foaming and drug solubilization, Colloids Surf. A Physicochem. Eng. Asp. 508 (2016) 159–166, https://doi.org/10.1016/j.colsurfa.2016.08.057.

[52] L. Stappers, J. Fransaer, AFM study of the incorporation of particles during electrodeposition, J. Electrochem. Soc. 154 (2007) D598–D611, https://doi.org/10.1149/1.2775165.

[53] V.S. Protsenko, F.I. Danilov, Kinetic model of composite coatings electrodeposition assuming irreversible adsorption of dispersed particles on a growing metal substrate, J. Electroanal. Chem. 918 (2022) 116463, https://doi.org/10.1016/j.jelechem.2022.116463.

[54] H. Bouazaze, S. Cattarin, F. Huet, M. Musiani, R.P. Nogueira, Electrochemical noise study of the effect of electrode surface wetting on the evolution of electrolytic hydrogen bubbles, J. Electroanal. Chem. 597 (2006) 60–68, https://doi.org/10.1016/j.jelechem.2006.08.003.

[55] J. Long, J. Zhang, L. Li, Y. Wen, X. Xu, F. Wang, S-doped NiFe layered double hydroxide with a large surface area for efficient oxygen evolution reaction, Int. J. Hydrogen Energy 90 (2024) 1424–1434, https://doi.org/10.1016/j.ijhydene.2024.09.320.

[56] F. Wang, T. Wang, S. Sun, Y. Xu, R. Yu, H. Li, One-step synthesis of Nickle iron-layered double hydroxide/reduced graphene oxide/carbon nanofibres composite as electrode materials for asymmetric supercapacitor, Sci. Rep. 8 (2018) 1–10, https://doi.org/10.1038/s41598-018-27171-0.

[57] V. Henri, E. Dantras, C. Lacabanne, A. Dieudonne, F. Koliatene, Thermal ageing of PTFE in the melted state: influence of interdiffusion on the physicochemical structure, Polym. Degrad. Stab. 171 (2020) 109053, https://doi.org/10.1016/j.polymdegradstab.2019.109053.

[58] H. Yu, A. Idesaki, A. Hiroki, S. Hasegawa, K. Hirota, Y. Maekawa, Effect of high-dose electron beam irradiation on thermal decomposition behavior of polytetrafluoroethylene (PTFE), radiation, Phys. Chem. 216 (2024) 111435, https://doi.org/10.1016/j.radphyschem.2023.111435.

[59] A. Angulo, P. van der Linde, H. Gardeniers, M. Modestino, D.Fernández Rivas, Influence of bubbles on the energy conversion efficiency of electrochemical reactors, Joule 4 (2020) 555–579, https://doi.org/10.1016/j.joule.2020.01.005.

[60] C.T.J. Low, R.G.A. Wills, F.C. Walsh, Electrodeposition of composite coatings containing nanoparticles in a metal deposit, Surf. Coat. Technol. 201 (2006) 371–383, https://doi.org/10.1016/j.surfcoat.2005.11.123.

[61] L. Deng, L. Jin, L. Yang, C. Feng, A. Tao, X. Jia, Z. Geng, C. Zhang, X. Cui, J. Shi, Bubble evolution dynamics in alkaline water electrolysis, EScience 5 (2025), https://doi.org/10.1016/j.esci.2024.100353.

[62] H. Liu, W. Chen, Electrodeposited Ni-Al composite coatings with high Al content by sediment co-deposition, Surf. Coat. Technol. 191 (2005) 341–350, https://doi.org/10.1016/j.surfcoat.2004.03.029.

[63] S. Yuan, Z. Wang, Y. Hao, C. Qi, J. Liu, Q. Wang, Design and preparation of 3D porous Ni–P/Ni integrated electrodes by electrodeposition for hydrogen evolution by electrolysis of water, J. Solid State Chem. 317 (2023) 123705, https://doi.org/10.1016/j.jssc.2022.123705.

[64] H. Liang, A.N. Gandi, C. Xia, M.N. Hedhili, D.H. Anjum, U. Schwingenschlögl, H. N. Alshareef, Amorphous NiFe-OH/NiFeP electrocatalyst fabricated at low temperature for water oxidation applications, ACS Energy Lett. 2 (2017) 1035–1042, https://doi.org/10.1021/acsenergylett.7b00206.

[65] L.M. Da Silva, L.A. De Faria, J.F.C. Boodts, Determination of the morphology factor of oxide layers, Electrochim. Acta 47 (2001) 395–403, https://doi.org/10.1016/S0013-4686(01)00738-1.

[66] W. Zheng, M. Liu, L.Y.S. Lee, Best practices in using foam-type electrodes for electrocatalytic performance benchmark, ACS Energy Lett. 5 (2020) 3260–3264, https://doi.org/10.1021/acsenergylett.0c01958.

[67] P. Tiwari, G. Tsekouras, K. Wagner, G.F. Swiegers, G.G. Wallace, A new class of bubble-free water electrolyzer that is intrinsically highly efficient, Int. J. Hydrogen Energy 44 (2019) 23568–23579, https://doi.org/10.1016/j.ijhydene.2019.07.100.

[68] T. Kadyk, D. Bruce, M. Eikerling, How to Enhance Gas Removal from Porous Electrodes ?, Nature Publishing Group (2016) 1–14, https://doi.org/10.1038/srep38780.

[69] S. Klaus, Y. Cai, M.W. Louie, L. Trotochaud, A.T. Bell, Effects of Fe electrolyte impurities on Ni(OH)2/NiOOH structure and oxygen evolution activity, J. Phys. Chem. C 119 (2015) 7243–7254, https://doi.org/10.1021/acs.jpcc.5b00105.

[70] S. Anantharaj, S. Kundu, S. Noda, The Fe Effect": a review unveiling the critical roles of Fe in enhancing OER activity of Ni and Co based catalysts, Nano Energy 80 (2021), https://doi.org/10.1016/j.nanoen.2020.105514.

[71] R. Iwata, L. Zhang, K.L. Wilke, S. Gong, M. He, B.M. Gallant, E.N. Wang, Bubble growth and departure modes on wettable/non-wettable porous foams in alkaline water splitting, Joule 5 (2021) 887–900, https://doi.org/10.1016/j.joule.2021.02.015.

[72] S.G. Quiroz, S. Cartagena, J.A. Calderón, Enhancement of oxygen evolution performance of water splitting at high current density by novel electrodeposited NiFe-LDH coatings, Electrochim. Acta 528 (2025), https://doi.org/10.1016/j.electacta.2025.146332.
[73] J. Niu, Y. Yue, C. Yang, Y. Wang, J. Qin, X. Zhang, Z.S. Wu, Ultrarapid synthesis Ni-Cu bifunctional electrocatalyst by self-etching electrodeposition for high-performance water splitting reaction, Appl. Surf. Sci. 561 (2021) 150030, https://doi.org/10.1016/j.apsusc.2021.150030.
[74] Q. Yang, C. Lv, Z. Huang, C. Zhang, Amorphous film of ternary Ni–Co–P alloy on Ni foam for efficient hydrogen evolution by electroless deposition, Int. J. Hydrogen Energy 43 (2018) 7872–7880, https://doi.org/10.1016/j.ijhydene.2018.03.003.
[75] Z. Guo, X. Wang, F. Yang, Z. Liu, Synergistic effect of Co and Fe bimetallic oxides/hydroxides composite structure as a bifunctional electrocatalyst for enhancing overall water splitting performance, J. Alloys Compd. 895 (2022) 162614, https://doi.org/10.1016/j.jallcom.2021.162614.
[76] S. Cartagena, J.A. Calderón, Corrosion of non-noble metal-based catalysts during oxygen evolution reaction under on/off operation, Corros. Sci. 205 (2022), https://doi.org/10.1016/j.corsci.2022.110437.
[77] J.D. Arias, S. Cartagena, J.A. Calderón, High-performance metal/particle catalytic coatings for hydrogen generation from alkaline water splitting, J. Mater. Sci. 60 (2025) 16069–16091, https://doi.org/10.1007/s10853-025-11436-x.
[78] J.O. Silva, S. Cartagena, J.A. Calderón, Novel electrodeposited NiFeP/Zn bifunctional catalytic coating for alkaline water splitting, Electrochim. Acta 451 (2023), https://doi.org/10.1016/j.electacta.2023.142299.
[79] X. Wang, W. Li, D. Xiong, L. Liu, Fast fabrication of self-supported porous nickel phosphide foam for efficient, durable oxygen evolution and overall water splitting, J. Mater. Chem. A Mater. 4 (2016) 5639–5646, https://doi.org/10.1039/c5ta10317g.
[80] T. Wang, X. Cao, L. Jiao, Ni2P/NiMoP heterostructure as a bifunctional electrocatalyst for energy-saving hydrogen production, EScience 1 (2021) 69–74, https://doi.org/10.1016/j.esci.2021.09.002.
[81] J. Li, Z.Y. Wang, N. Deng, C.X. Li, Z.G. Guo, J.B. He, In situ formation of a nickel-iron-sulfur bifunctional catalyst within a porous polythiophene coating for water electrolysis, Int. J. Hydrogen Energy 47 (2022) 17630–17639, https://doi.org/10.1016/j.ijhydene.2022.03.242.
[82] G. Zhang, H. Ge, L. Zhao, J. Liu, F. Wang, S. Fan, G. Li, NiMn1.5PO4 thin layer supported on Ni foam as a highly efficient bifunctional electrocatalyst for overall water splitting, Electrochim. Acta 367 (2021) 137567, https://doi.org/10.1016/j.electacta.2020.137567.
[83] J. Zhou, C. Huang, Q. Zhou, Y. Xie, L. Yang, L. Yu, Y. Yu, Electronic structure regulation of nickel phosphide for efficient overall water splitting, Inorg. Chem. 61 (2022) 9318–9327, https://doi.org/10.1021/acs.inorgchem.2c01070.
[84] S. Kroy, W.G. Shin, Understanding the effect of electrode thicknesses on bubble detachment and Hydrogen Evolution Reaction (HER) in water electrolysis using bare nickel foam, J. Power Sources 613 (2024), https://doi.org/10.1016/j.jpowsour.2024.234820.
[85] K.M. Cho, P.R. Deshmukh, W.G. Shin, Hydrodynamic behavior of bubbles at gas-evolving electrode in ultrasonic field during water electrolysis, Ultrason. Sonochem. 80 (2021) 105796, https://doi.org/10.1016/j.ultsonch.2021.105796.
[86] M.M. Saleh, Simulation of oxygen evolution reaction at porous anode from flowing electrolytes, J. Solid State Electrochem. 11 (2007) 811–820, https://doi.org/10.1007/s10008-006-0227-7.